

RESEARCH ARTICLE

Effect of Iron Contamination and Polysilicon Gettering on the Performance of Polysilicon-Based Passivating Contact Solar Cells

Zhongshu Yang¹  | Rabin Basnet¹ | Chris Samundsett¹ | Sieu Pheng Phang¹ | Thien Truong^{1,2} | Di Kang¹ | Wensheng Liang¹ | Anh Dinh Bui¹  | Wei Wang¹ | Tien T. Le¹  | Daniel Macdonald¹ | AnYao Liu¹ 

¹School of Engineering, The Australian National University, Canberra, Australian Capital Territory, Australia | ²Materials, Chemical, and Computational Science (MCCS) Directorate, National Renewable Energy Laboratory (NREL), Golden, Colorado, USA

Correspondence: Zhongshu Yang (zhongshu.yang@anu.edu.au) | AnYao Liu (anyao.liu@anu.edu.au)

Received: 22 February 2024 | **Revised:** 15 October 2024 | **Accepted:** 11 November 2024

Funding: This work has been supported by the Australian Renewable Energy Agency (ARENA) through the Australian Centre for Advanced Photovoltaics (ACAP), project 2022/TRAC004.

Keywords: impurity gettering | iron contamination | polysilicon | silicon solar cell

ABSTRACT

Over the past decade, silicon solar cells with carrier-selective passivating contacts based on polysilicon capping an ultra-thin silicon oxide (commonly known as TOPCon or POLO) have demonstrated promising efficiency potentials and are regarded as an evolutionary upgrade to the PERC (passivated emitter and rear contact) cells in manufacturing. The polysilicon-based passivating contacts also exhibit excellent gettering effects that relax the wafer and cleanroom requirements to some extent. In this work, we experimentally explore the impact of bulk iron contamination and polysilicon gettering on the passivation quality of the polysilicon/oxide structure and the resulting solar cells performance. Results show that both *n*- and *p*-type polysilicon/oxide passivating contacts are not affected by iron gettering, demonstrating robust and stable passivation quality. However, for a very high bulk iron contamination ($1 \times 10^{13} \text{ cm}^{-3}$), the accumulated iron in the *p*-type lightly boron-doped emitter in crystalline silicon would degrade the emitter saturation current density. This can cause a reduction in both open-circuit voltage and short-circuit current. Meanwhile, this very high iron content ($1 \times 10^{13} \text{ cm}^{-3}$) can further degrade the fill factor and temperature coefficient of the cells. On the other hand, for an initial iron content of $2 \times 10^{12} \text{ cm}^{-3}$, which should be well above the iron level in the current industrial Czochralski silicon wafers, the resulting cells demonstrate similar performance as the control group with no intentional iron contamination. This work brings attention to both the benefits of polysilicon gettering effects as well as the potential degradation due to the accumulation of metal impurities in the *p*-type emitter region.

1 | Introduction

Photovoltaic (PV) technology is a key contributor to renewable energy sources, and crystalline silicon (c-Si) based solar cells take up approximately 95% of the current PV market share [1]. As the predominant passivated emitter and rear cell (PERC) architecture approaches its efficiency limit in industrial mass production, the PV industry is transitioning to new technologies

of both high efficiency and low cost. Cells with passivating contacts based on a polysilicon (poly-Si) layer and an ultra-thin silicon oxide (SiO_x) interlayer, also known as tunnel oxide passivated contacts (TOPCon) or polysilicon on oxide (POLO), have demonstrated impressive improvements in the power conversion efficiency (PCE) in the past decade [2–4]. Meanwhile, the excellent compatibility with the existing fabrication techniques and processes of PERC makes the poly-Si/ SiO_x route

an evolutionary upgrade to the PERC solar cell manufacturing platform [5, 6].

Similar to *p*-type PERC solar cells involving an inherent phosphorus diffusion gettering process during the front emitter formation, the poly-Si/SiO_x-based solar cells benefit from the gettering effect of the poly-Si/SiO_x on the rear side [7–10]. This relaxes the c-Si wafer requirements for cell production to some extent, as certain fast-diffusion metal impurities can be gettered during the cell fabrication process. Among these, iron (Fe) is one of the most common but detrimental metal impurities in silicon device [11–13]. Fe contamination is known to cause a reduction in minority carrier effective lifetime, which can be characterized by Shockley Read Hall (SRH) statistics [14, 15]. In this case, Fe is known to be less harmful in *n*-type than the *p*-type c-Si, due to its asymmetric capture cross sections for the electrons and holes [16].

Despite the potential efficiency gains from the gettering effects of the poly-Si/SiO_x passivating contacts, as simulated in [17, 18] based on experimental gettering results, it is not entirely certain how the application of polysilicon gettering affects the poly-Si/SiO_x passivation quality and the resulting cell performance. According to previous findings [19], majority of the gettered metal impurities by the poly-Si/SiO_x passivating contacts go through the ultra-thin SiO_x interlayer and gather in the heavily doped poly-Si layers, which is the main gettering sink. A smaller amount of the gettered metals accumulate in the in-diffused c-Si surface region. These raise concerns about whether or not the gettered metal impurities would degrade the performance of the poly-Si/SiO_x passivating contacts. The first concern is the potential accumulation of metal impurities in the in-diffused c-Si surface region, which may enhance the defect-mediated carrier recombination [13, 20] other than the bulk Auger recombination near the SiO_x interface [21]. The other concern is the potential damage to the interfacial SiO_x interlayer from the gettering process. The interfacial SiO_x layer is an effective barrier for dopants [22], as well as for metal impurities [17]. Based on our previous work [17], during the poly-Si/SiO_x gettering process, metal impurities would move through the interfacial SiO_x layer either by direct diffusion or through pinholes. The diffusion behavior of Fe atoms through the SiO_x interlayers [23, 24], therefore, may potentially introduce SiO_x/c-Si interface damage and affect the passivation quality. Preliminary results reported by Liu et al. indicate that the poly-Si/SiO_x gettering of Fe does not affect the passivation quality of the poly-Si/SiO_x structure [8]. However, the results were only based on lifetime (i.e., implied open-circuit voltage) measurements from *p*-type c-Si substrates with a low resistivity, where the effective lifetimes may be affected by other recombination sources such as intrinsic recombination. Besides, a limited number of scenarios were considered, and the impact on cell performance was not examined in [8]. In addition, it is unclear whether the accumulation of Fe in the poly-Si/SiO_x structure would affect the hydrogenation response or the poly-Si/SiO_x firing stability.

Additionally, the impact of metal impurities has been experimentally studied on *p*-type aluminum-back surface field (Al-BSF) and PERC solar cells [25–27], but not on the *n*-type poly-Si/SiO_x-based solar cells. Simulation studies solely focused on the SRH recombination properties of various common metal impurities

in *n*-type c-Si bulk (for example, in [28, 29]). However, it is essential to note that metal contamination may cause additional degradation to cell performance. For example, it was reported that Fe contamination would affect the *p*-type emitter quality [20, 30]. Meanwhile, unlike *p*-type c-Si [31], there is no direct method to detect bulk Fe concentration in *n*-type c-Si due to the lack of metastable iron–boron (FeB) pairs. This makes it more challenging to evaluate the impact of Fe contamination and gettering on *n*-type solar cells.

Therefore, in this work, we aim to experimentally examine the impact of bulk Fe contamination and subsequent gettering during cell processing (from both *n*-type poly-Si/SiO_x on the rear and *p*-type emitter on the front) on the performance of *n*-type poly-Si/SiO_x-based solar cells. We first compared and explored the impact of Fe gettering on the passivation quality and firing stability of both *n*-type (phosphorus-doped) and *p*-type (boron-doped) poly-Si/SiO_x structures by thermal diffusion. Afterwards, *n*-type front junction (*n*-FJ) poly-Si/SiO_x-based solar cells with different initial bulk Fe concentrations ($[Fe_i]_{initial}$) were fabricated and characterized, to compare the power loss mechanisms from current–voltage (IV), quantum efficiency (QE), and Suns-V_{oc} measurements. Lastly, the temperature coefficients (TC) of open-circuit voltage (V_{oc}) were measured and compared. Besides high-quality float-zone (FZ) silicon control samples, samples with two different initial bulk Fe concentrations were prepared by ion implantation and annealing: $[Fe_i]_{initial} = 2 \times 10^{12} \text{ cm}^{-3}$ and $[Fe_i]_{initial} = 1 \times 10^{13} \text{ cm}^{-3}$, which represent the contamination levels in Czochralski (CZ) Si wafers in the tail region of the ingot (highest in the whole ingot) [32] and in multicrystalline Si wafers from bottom or top part of the ingot (very high contamination level as an example) [33], respectively. These results help to demonstrate the application of poly-Si/SiO_x passivating contacts on lower purity c-Si wafers (with high Fe contents), the benefits and limitations of the poly-Si/SiO_x gettering effects, and the impact of Fe contamination on the performance of *n*-type poly-Si/SiO_x-based solar cells.

2 | Experimental

2.1 | Preparation of Fe-Contaminated Samples

A flowchart outlining the experimental procedure for preparing silicon wafers with known bulk Fe contamination levels is shown in Figure 1A. After saw damage etching in a tetramethylammonium hydroxide (TMAH) solution, high-quality FZ c-Si wafers were subjected to ion implantation with Fe atoms. After standard RCA cleaning, the implanted c-Si wafers went through high-temperature annealing in dry oxygen and subsequent nitrogen ambient gas. Details of the Fe implantation and distribution annealing process, which minimizes implantation damage and Fe precipitation in the c-Si wafers, can be found in [19, 34]. Besides control samples that went through the same annealing process as the Fe contaminated samples, samples with two different Fe doses were prepared, resulting in uniform volumetric interstitial Fe concentrations of $[Fe_i] = (2 \pm 0.2) \times 10^{12} \text{ cm}^{-3}$ and $[Fe_i] = (1 \pm 0.1) \times 10^{13} \text{ cm}^{-3}$.

Samples of different bulk wafer types and resistivities were prepared: *p*-type 2.5 Ωcm FZ wafers for bulk Fe concentration

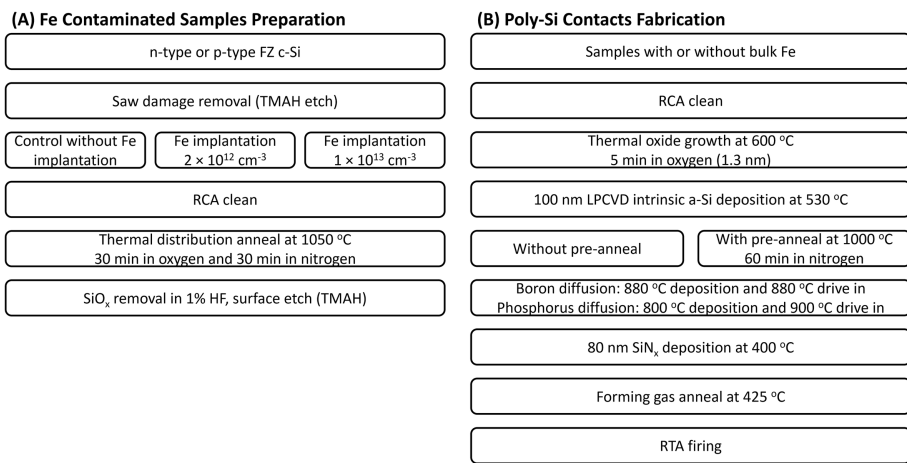


FIGURE 1 | Plot (A) shows the experimental procedure flowchart for Fe contaminated sample preparation and (B) is the flow chart for the poly-Si/ SiO_x symmetrical lifetime samples fabrication procedure.

monitoring; *n*- and *p*-type $100\Omega\text{cm}$ FZ wafers for the measurement of passivation quality and firing stability; and *n*-type $2\Omega\text{cm}$ FZ wafers for *n*-type poly-Si/ SiO_x -based solar cell fabrication. Note that all the wafers featured mechanically non-polished pseudo planar surfaces after TMAH etching except the *p*-type $100\Omega\text{cm}$ FZ wafers (mechanically polished mirror-like surfaces), as observed under optical microscope.

Before further processing, the thermally grown oxide layers from the distribution anneal were removed by a 1% hydrofluoric acid (HF) solution, followed by a shallow surface etching in TMAH solution to remove any potential near-surface implantation damage.

2.2 | Fabrication of Poly-Si/ SiO_x Symmetrical Lifetime Samples

As shown by the experimental flowchart for poly-Si/ SiO_x fabrication procedure in Figure 1B, the samples with or without bulk Fe contamination first went through thermal oxidation at 600°C for 5 min in dry oxygen ambient after RCA cleaning. The thickness of the ultra-thin SiO_x layer was $1.3 \pm 0.2 \text{ nm}$ as measured by spectroscopic ellipsometry. Afterwards, about 100-nm-thick intrinsic amorphous silicon (a-Si) layers were deposited on both sides by using a Tempress low-pressure chemical vapor deposition (LPCVD) system at 530°C . An additional pre-annealing step at 1000°C was added for one group of the samples before the diffusion step, in order to achieve better passivation quality as reported in [35]. All of the samples were then subjected to an ex situ diffusion process using BBr_3 or POCl_3 as the diffusion source in quartz tube furnaces. After the diffusion process, boron silicate glass (BSG) or phosphosilicate glass (PSG) on the wafer surfaces was removed by a diluted HF solution. The samples were then coated with 80-nm SiN_x layers on both sides using an Oxford PlasmaLab 100 plasma-enhanced chemical vapor deposition (PECVD) tool, followed by a hydrogenation process of a forming gas anneal (FGA) at 425°C for 30 min. Additionally, a firing treatment was performed on the samples for the firing stability test, using a rapid thermal annealing (RTA) tool, with ramp-up and

ramp-down rate of 30°C and $60^\circ\text{C}/\text{s}$, respectively, and a peak on-sample temperature of 900°C .

2.3 | Fabrication of *n*-FJ Poly-Si/ SiO_x -Based Solar Cells

The *n*-FJ poly-Si/ SiO_x -based solar cells in this work were made from *n*-type $2\Omega\text{cm}$ high-quality FZ wafers and have a designed cell area of $2 \times 2 \text{ cm}^2$. After defining cell area through photolithography, bulk Fe contamination was intentionally introduced into the c-Si substrates via ion implantation and thermal annealing, as described previously, resulting in two initial bulk Fe concentrations: $[\text{Fe}_1] = (2 \pm 0.2) \times 10^{12} \text{ cm}^{-3}$ and $[\text{Fe}_2] = (1 \pm 0.1) \times 10^{13} \text{ cm}^{-3}$. It is worth noting that, unlike the lifetime sample preparation in Section 2.1, only the active cell areas on the front side of the Si substrate were subjected to HF etching and shallow surface etching in TMAH solution for removing any potential damage due to ion implantation. The rear side SiO_x from high temperature Fe distribution annealing was retained as a diffusion barrier to subsequent boron diffusion process.

Figure 2A illustrates the cross section of the *n*-FJ poly-Si/ SiO_x -based solar cell structure, and the solar cell fabrication process is outlined in Figure 2B. The front side of the solar cells features a textured surface (random-pyramids) with a boron-doped homogenous *p*-type emitter. The *p*-type emitter was formed by BBr_3 thermal diffusion at 900°C and subsequent *in-situ* oxidation step, resulting in a sheet resistance of $180 \Omega/\text{sq}$. The front *p*-type emitter was passivated by a 20-nm-thick aluminum oxide (AlO_x) layer using plasma-enhance atomic layer deposition (PE-ALD) and capped with a 60-nm-thick silicon nitride (SiN_x) layer using PECVD for antireflection coating. The front $\text{AlO}_x/\text{SiN}_x$ stack was chemically etched through for contact opening, and metal fingers were formed with a stack of chromium/palladium/silver ($\text{Cr}/\text{Pd}/\text{Ag}$) by thermal evaporation. The rear side of the solar cells features a planar surface with full area phosphorus-doped poly-Si/ SiO_x passivating contact. The *n*-type poly-Si/ SiO_x passivating contact was formed by an ultra-thin thermal SiO_x

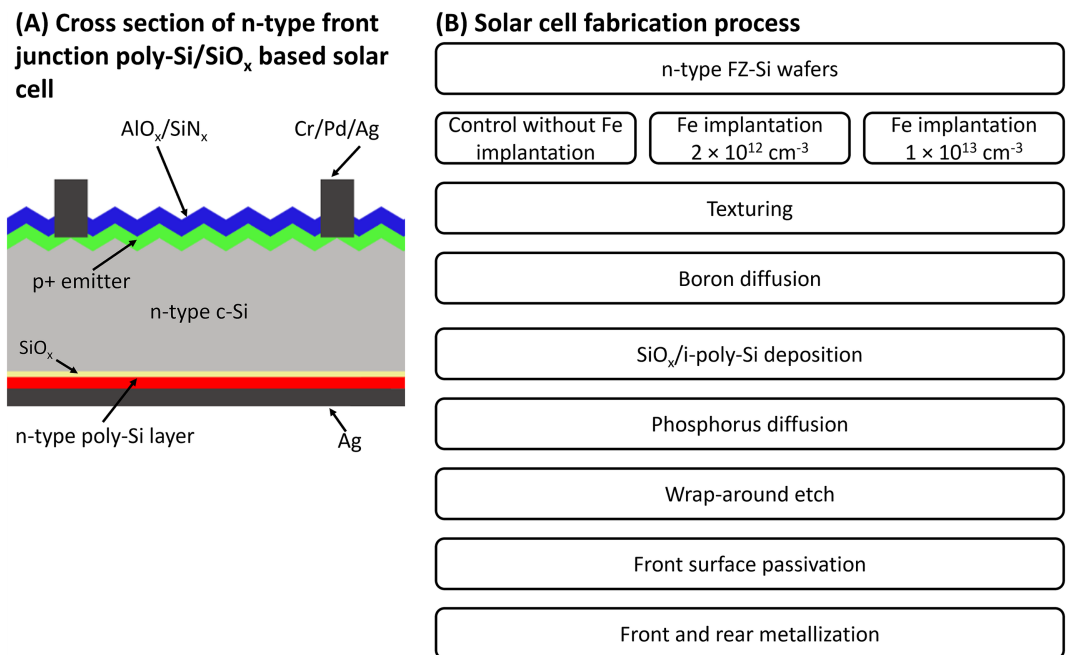


FIGURE 2 | Plot (A) shows the schematic cross section (not to scale) of the *n*-type front junction poly-Si/SiO_x-based solar cell, and (B) is the experimental flow chart for the solar cell fabrication process.

interlayer and phosphorus-doped poly-Si layer from LPCVD and POCl₃ diffusion, the exact same process as used in the symmetrical lifetime samples described above. After the removal of the PSG layer, rear metallization was realized by thermally evaporated Ag.

2.4 | Characterization Methods

The bulk Fe concentrations in the poly-Si/SiO_x symmetrical lifetime samples (including *n*- and *p*-type 100 Ωcm wafers) were estimated from measuring the co-processed *p*-type 2.5 Ωcm samples, which allow the measurements of bulk Fe concentration through FeB pair association-dissociation methods [31, 36, 37]. Effective lifetimes before and after illumination to break the FeB pairs were measured using a Sinton Instruments WCT-120 lifetime tester [38], and the bulk Fe concentration measurement was not affected by the non-uniform [Fe_i] distribution in this work [39]. The surface recombination current density (J_0) is derived from the measured effective lifetime curves on *n*- and *p*-type 100 Ωcm wafers, according to the method of Kane and Swanson [40] with band gap narrowing [41], and the recent radiative [42] and Auger [43] recombination models.

The electrically active dopant concentrations of the poly-Si/SiO_x and *p*-type front emitter of the solar cells were measured by electrochemical capacitance-voltage (ECV) technique (WEP Wafer Profile CVP21). The sheet resistances were measured using a 4-point probe tool. The crystallinity properties of the poly-Si layer were examined by grazing-incidence X-ray diffraction (GIXRD) spectroscopy measurement (PANalytical X'Pert PRO MRD system), and the grain size was calculated using the Debye-Scherrer formula [44].

The illuminated IV and Suns-V_{oc} curves of the poly-Si/SiO_x-based solar cells were measured on the full 2 × 2 cm² cell area including the metal fingers by a Sinton Instruments FCT-450 tool, with the non-cell area (6-mm gap between adjacent cells) being shadowed. The QE responses of the cells were measured using a QE-R quantum efficiency system from Enlitech. The photoluminescence (PL) images of the cells were captured using an LIS-R1 PL imaging apparatus from BT imaging. The TC of V_{oc} of the cells was measured using solar simulator model WAVELABS SINUS-220 equipped with a temperature control system made in-house.

3 | Results

3.1 | Symmetric Poly-Si/SiO_x Lifetime Samples

3.1.1 | Gettering Effectiveness of Poly-Si/SiO_x Structures

The measured remaining bulk Fe concentrations at different stages of the poly-Si/SiO_x formation process are shown in Figure 3. All samples were subjected to an additional pre-annealing step before diffusion and firing to achieve better surface passivation [35]. The poly-Si deposition and pre-annealing steps exhibit little gettering effects on their own, with over 90% of the initial Fe atoms still remaining in the c-Si bulk before the diffusion process. This results from the insufficient gettering effect of the thin intrinsic poly-Si layers [8, 45]. Moreover, the overall gettering effect of the intrinsic poly-Si/SiO_x is further restrained by the limited thermal budget during the cooling down period (10°C/min) of the pre-annealing step and the blocking effect of the thermal SiO_x interlayer [17].

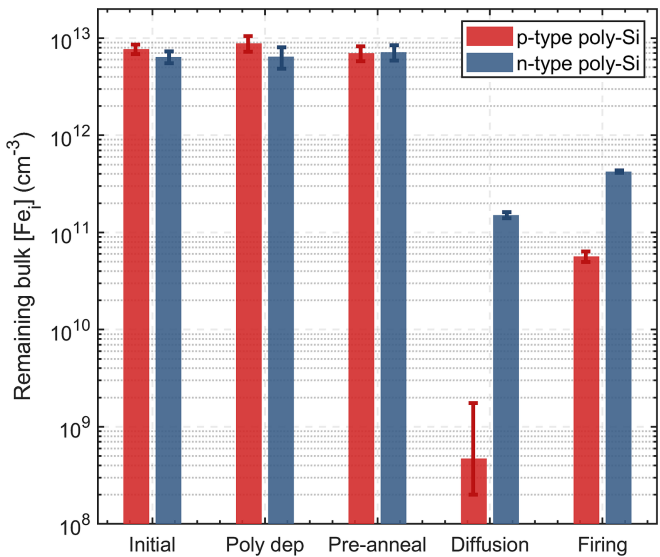


FIGURE 3 | Measured remaining bulk Fe concentrations in the *p*-type 2.5 Ωcm samples with double-side poly-Si/SiO_x at different poly-Si/SiO_x fabrication stages: initial stage; after intrinsic poly-Si deposition by LPCVD; after pre-annealing at 1000°C for 60 min; after diffusion (POCl₃ for *n*-type poly-Si/SiO_x and BBr₃ for *p*-type poly-Si/SiO_x); and after firing at an on-sample peak temperature of 900°C for 5 s.

It is clear from Figure 3 that after the diffusion process, very effective gettering is achieved, with about 99% of the implanted Fe atoms in the c-Si bulk being removed from the c-Si bulk (see Figure S1 for lifetime spectra). After the formation of phosphorus-doped poly-Si/SiO_x structure, about 1% of the initial bulk Fe atoms remains in the c-Si bulk, while for the boron-doped poly-Si/SiO_x, there are only about 0.01% of the initial bulk Fe atoms remaining. This can be attributed to the excellent gettering of boron-rich layer (BRL) formed in the boron diffusion process [8, 46]. The gettering effectiveness of the poly-Si/SiO_x in Figure 3 is consistent with our previous findings that the *ex situ* BBr₃ diffused boron-doped poly-Si/SiO_x exhibit stronger gettering effects than phosphorus-doped poly-Si/SiO_x [18]. Details about the gettering mechanisms of phosphorus- or boron-doped poly-Si/SiO_x can be found in [8, 18, 45, 46]. Note that the gettering effectiveness discussed here results from samples with symmetrical double-side poly-Si/SiO_x, while typical poly-Si/SiO_x-based solar cells only benefit from single-side poly-Si/SiO_x gettering.

It is worth noting that despite the different gettering strengths of the *n*- and *p*-type poly-Si/SiO_x, the absolute amount of the gettered Fe atoms accumulating in the poly-Si layer is similar. For example, the accumulated Fe concentrations in the *n*- and *p*-type poly-Si layer in Figure 3 are both at a level around $2 \times 10^{16} \text{ cm}^{-3}$. This is because that after the diffusion process, about 99% (phosphorus-doped) or 99.99% (boron-doped) of the initial Fe concentration is relocated into the poly-Si/SiO_x structure, and in that case, the gettered Fe concentrations mainly depend on the initial bulk Fe concentrations, which are the same for both types.

Although the poly-Si/SiO_x can remove most of the initial bulk Fe atoms, an increase of the remaining bulk Fe concentration is observed after the firing step for the samples with either *p*- or *n*-type poly-Si/SiO_x structure (see Figure 3). A diffusion-limited segregation gettering model [19] was applied to simulate the

redistribution of Fe atoms during the firing process for the given temperature-time profile. The values of the blocking effect of the SiO_x interlayer and the gettering strength of the poly-Si/SiO_x (*n*-type) were assumed based on our previous work of similar process conditions [17, 18]. Based on the assumed parameters, simulation results indicate a less than 1% change of the remaining bulk Fe concentration after the applied firing process from the previous diffusion step, which is not consistent with the experimental results in Figure 3 that the bulk Fe concentrations increase by 180% after firing for *n*-type poly-Si. Hence, the increasing bulk Fe concentration after the firing process is more likely to result from external contamination (such as potential contamination from the RTP tool or from the contaminated SiN_x layers), which breaks the balance of the ratio of Fe concentrations in the poly-Si layer and in the bulk. Similar findings were also observed in Ref [47] that the remaining bulk Fe concentration increases with higher firing temperatures for both AlO_x and SiN_x passivated samples and it was suggested that Fe contamination was introduced during the firing step, similar to our speculation here.

3.1.2 | Impact of Gettering on Poly-Si/SiO_x Passivation

As shown earlier in Figure 3, after thermal diffusion, more than 99% of the bulk Fe atoms have been gettered, meaning that they have been relocated to the heavily doped poly-Si layers (main gettering region) and the in-diffused surface c-Si regions [19]. It is essential, therefore, to assess the impact of such high Fe accumulation on the poly-Si/SiO_x passivation quality. Figure 4 illustrates the measured single-side J₀ values on the *n*- or *p*-type 100 Ωcm substrates with different initial Fe concentrations. The J₀ values are extracted from the effective lifetime curve on samples without hydrogenation treatment at an injection level of $5 \times 10^{15} \text{ cm}^{-3}$. These samples are well passivated by double-side boron- or phosphorus-doped poly-Si/SiO_x with or without a pre-annealing step before the diffusion process. Note that the J₀ values of the poly-Si/SiO_x

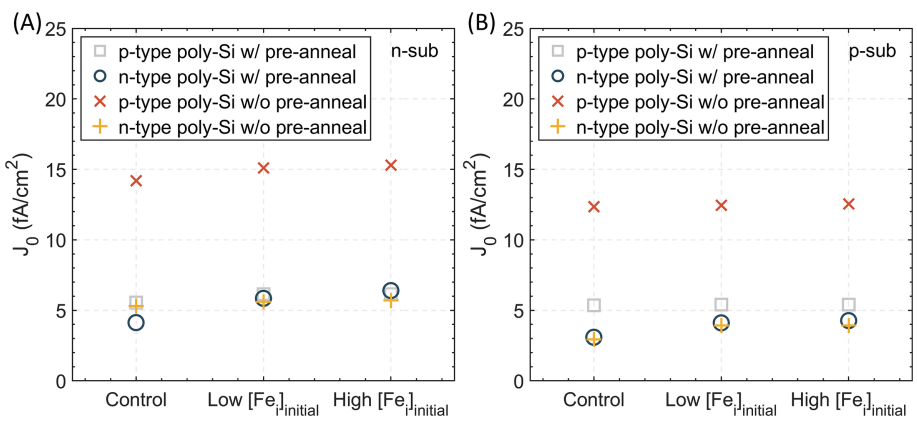


FIGURE 4 | Measured single-side surface recombination current density (J_0) for boron- and phosphorus-doped poly-Si/SiO_x with or without pre-annealing on the (A) n-type and (B) p-type 100 Ωcm substrates. Control, low $[Fe_i]_{\text{initial}}$, and high $[Fe_i]_{\text{initial}}$ denote control samples and samples with initial bulk Fe concentrations of $2 \times 10^{12} \text{ cm}^{-3}$ and $1 \times 10^{13} \text{ cm}^{-3}$, respectively. The J_0 values were measured on samples without hydrogenation treatment.

on n-type substrates are consistently larger than the p-type substrates, which can be attributed to the different surface features of these two types of substrates: p-type 100 Ωcm wafers feature mechanically polished mirror-like surfaces while the n-type 100 Ωcm wafers were simply chemically polished to pseudo planar surfaces.

As shown in Figure 4, the phosphorus-doped poly-Si/SiO_x exhibit good passivation quality with J_0 values of around 5 fA/cm², and the pre-annealing step barely affects the passivation performance. The ECV profiles of the electrically active phosphorus concentration (see Figure S2) present slightly heavier in-diffusion for the samples without pre-annealing compared to the ones with pre-annealing. This can be explained by the fact that the interfacial oxide acts as an effective diffusion barrier for phosphorus [22]. Additionally, high-temperature pre-annealing can further enhance its blocking effect by increasing the interfacial oxide stoichiometry [48]. Nevertheless, as shown by the results in Figure 4, the pre-annealing step does not improve the passivation quality of the n-type poly-Si/SiO_x despite the slightly shallower phosphorus in-diffusion, which can be attributed to the trade-off between Auger recombination and electric field passivation.

On the other hand, the boron-doped poly-Si/SiO_x demonstrates a reduced passivation quality without pre-annealing, with J_0 values of 12–15 fA/cm². This is close to the reported J_0 values of the boron-doped poly-Si/SiO_x with thermal oxide and ex-situ BBr₃ diffusion [6]. In contrast to phosphorus-doped poly-Si/SiO_x, a pre-annealing step can significantly improve the passivation quality of boron-doped poly-Si/SiO_x, resulting in J_0 values of around 5 fA/cm². The details of the challenges facing boron-doped poly-Si/SiO_x and one mitigation approach deploying a pre-annealing step, as applied in this study, can be found in Refs [35, 49], respectively. The electrically active boron profiles exhibit no difference between the samples with and without pre-annealing, as shown in Figure S2, which is consistent with the results from [35, 50].

As the initial bulk Fe concentration increases (i.e., more Fe atoms are gettertered into the poly-Si/SiO_x), there is only a slight increment of the J_0 values observed (1–2 fA/cm²) in Figure 4. However, taking into account the measurement uncertainties, this difference in J_0 values is too minor to conclude that the Fe

atoms gettertered by the doped poly-Si/SiO_x would significantly degrade the passivation performance. In addition, rather high bulk Fe concentrations from intentional contamination are examined in this work, while lower Fe concentrations (well below 10^{12} cm^{-3}) are expected in the current CZ-Si wafers [32, 51]. Therefore, the impact of Fe getterting on the passivation effect of poly-Si/SiO_x is expected to be negligible.

Lastly, we measured and compared the crystallinity of the poly-Si layer on the samples with different initial bulk Fe concentrations after POCl₃ or BBr₃ diffusion, due to potential metal-induced crystallization of the poly-Si layers [52, 53]. Figure S3 shows the calculated grain sizes of the poly-Si layers from XRD measurement. In general, the boron-doped poly-Si layers have a smaller grain size compared to the phosphorus-doped poly-Si layers. However, no noticeable difference can be observed for the samples with different initial bulk Fe concentrations. This indicates that within the XRD detection limit, the presence of Fe atoms, and the Fe concentrations examined in this work, may not affect the poly-Si layer crystallization process.

3.1.3 | Impact of Gettering on Poly-Si/SiO_x Firing Stability

The firing stability of the poly-Si/SiO_x was studied in recent years [54–59], and the accumulation of hydrogen atoms at the SiO_x interlayer was suspected to be the reason for the passivation degradation after a firing process. The hydrogen-rich capping layers (e.g., AlO_x or SiN_x layers) were reported to present decent gettering effects [60, 61], although the hydrogen atoms should not affect the gettering effectiveness or the Fe diffusivity as suggested in [62]. However, it is unclear whether or not the accumulation of Fe atoms in the poly-Si layer would affect the hydrogenation response or the poly-Si/SiO_x firing stability.

Figure 5 presents the measured single-side J_0 values of the symmetrical double-side poly-Si/SiO_x coated samples with various initial bulk Fe concentrations at different hydrogenation stages: after diffusion, after SiN_x deposition and FGA, and after firing process. Note that the samples in Figure 5 all underwent

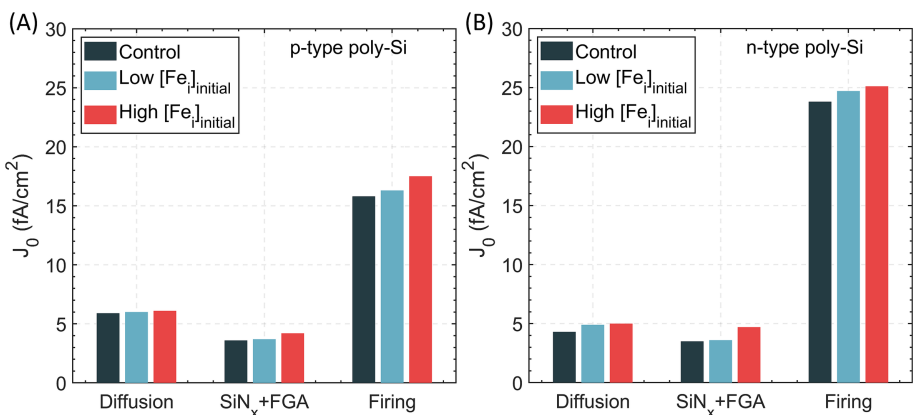


FIGURE 5 | Measured single-side surface recombination current density (J_0) for (A) p-type and (B) n-type poly-Si/SiO_x contacts at different stages: after diffusion (POCl₃ for n-type poly-Si and BBr₃ for p-type poly-Si); after SiN_x deposition and FGA at 425°C for 30 min; and after firing at an on-sample peak temperature of 900°C for 5 s.

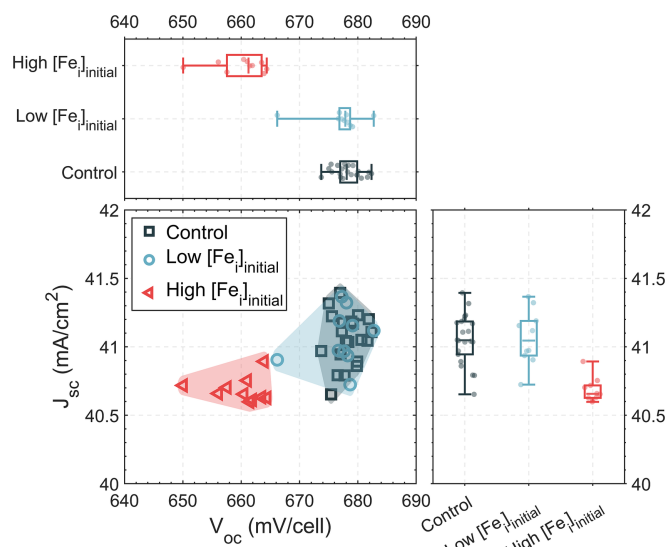


FIGURE 6 | Measured open-circuit voltage (V_{oc}) and short-circuit current density (J_{sc}) of the n-type front junction poly-Si/SiO_x-based solar cells with no (control), low ($[Fe]_{initial} = 2 \times 10^{12} \text{ cm}^{-3}$), and high ($[Fe]_{initial} = 1 \times 10^{13} \text{ cm}^{-3}$) Fe implantation doses.

pre-annealing for better passivation quality. After thermal diffusion, the poly-Si/SiO_x demonstrates good passivation effect with J_0 values of about 5 fA/cm². After SiN_x deposition and FGA, the surface passivation of the poly-Si/SiO_x improves slightly for both boron- and phosphorus-doped poly-Si/SiO_x, consistent with the previous results [63]. The J_0 values then exhibit obvious degradation after the firing process (about 15–18 fA/cm² for boron-doped poly-Si/SiO_x and 23–25 fA/cm² for phosphorus-doped poly-Si/SiO_x). It is worth noting that a firing temperature of 900°C is higher than the current typical firing temperature used in mass production, due to evolving metal paste. Therefore, the RTA process with a peak temperature of 900°C represents an extreme case, and the actual impact of firing could be less significant.

Similar to the impact of gettering on passivation in Figure 4, Figure 5 shows that there is only a minor increment of the J_0 values of 1–2 fA/cm² with increasing initial bulk Fe concentrations for the samples at different stages. Nevertheless, considering the measurement uncertainty, we cannot conclude that there

is a significant impact of the presence of gettered Fe atoms on the hydrogenation response or the firing stability of the poly-Si/SiO_x.

3.2 | n-FJ Poly-Si/SiO_x-Based Solar Cells

In this section, we explore the impacts of bulk Fe contamination and process-induced gettering (from both n-type poly-Si/SiO_x on the rear and p-type emitter on the front) on the performance of n-FJ poly-Si/SiO_x-based solar cells, by fabricating cells with different initial bulk Fe concentrations.

3.2.1 | Current-Voltage and Quantum Efficiency Measurements

Figure 6 shows the open-circuit voltage (V_{oc}) and short-circuit current density (J_{sc}) of the resulting cells. As shown in Figure 6,

the cells with a low $[Fe_i]_{\text{initial}}$ ($2 \times 10^{12} \text{ cm}^{-3}$) have similar V_{oc} and J_{sc} values as the control cells, while the cells with a high $[Fe_i]_{\text{initial}}$ ($1 \times 10^{13} \text{ cm}^{-3}$) exhibit both lower V_{oc} and J_{sc} values, suggesting obviously lower cell efficiency potentials. The cell efficiencies are not shown here, as the fabricated cells suffered from pronounced series resistance issues.

To understand the current loss of the n -FJ poly-Si/SiO_x-based solar cells, internal quantum efficiency (IQE) of the cells was derived from the spectral response and reflectance measurements, as shown in Figure 7A. The external quantum efficiency and integrated J_{sc} are shown in Figure S4. The difference in the IQE curves with different initial Fe concentrations comes from both the short and long wavelength response of the IQE curves. The IQE values of the cells at a specific wavelength of 400 and 1000 nm are shown in Figure 7B,C for better clarity.

The IQE values at a short wavelength of 400 nm represent front surface recombination and recombination in the emitter region, due to the shallow absorption of photons of a 400-nm wavelength in c-Si. The results in Figure 7B clearly show a reduction of IQE values at 400 nm with increasing initial bulk Fe concentrations. This can be attributed to the increased recombination in the emitter region, as explained as follows.

Figure 7D illustrates the double-side surface recombination current density J_0 calculated from the effective lifetime curves of the cell precursors before metallization. It is worth noting that the active cell area is slightly smaller than the coil detection area of the lifetime tester, and hence the non-cell area may alter the measured effective lifetime curve, which can result in slightly underestimated J_0 values especially for the cells with higher Fe contamination. However, as shown in Figure 7D, there is an obvious trend of increasing J_0 values with increasing initial bulk Fe concentrations. According to the previous results in Section 3.1.2, the rear side poly-Si/SiO_x passivation is resilient to Fe gettering. Therefore, the difference in the double-side J_0 values in Figure 7D is attributed to the front-side p -type emitter. Furthermore, the trend of increasing J_0 with increasing initial bulk Fe concentration is not observed in p -type front junction poly-Si/SiO_x-based solar cells (homogenous n -type emitter passivated with SiN_x on the front side and p -type poly-Si/SiO_x passivating contact on the rear side), as shown in Figure S5. The reasons are explained below.

The Fe contamination level in the p -type emitter increases with increasing initial bulk Fe concentrations, as a result of boron diffusion gettering [64] during the cell processing. According to [20, 30], for the c-Si wafer bulk with an initial

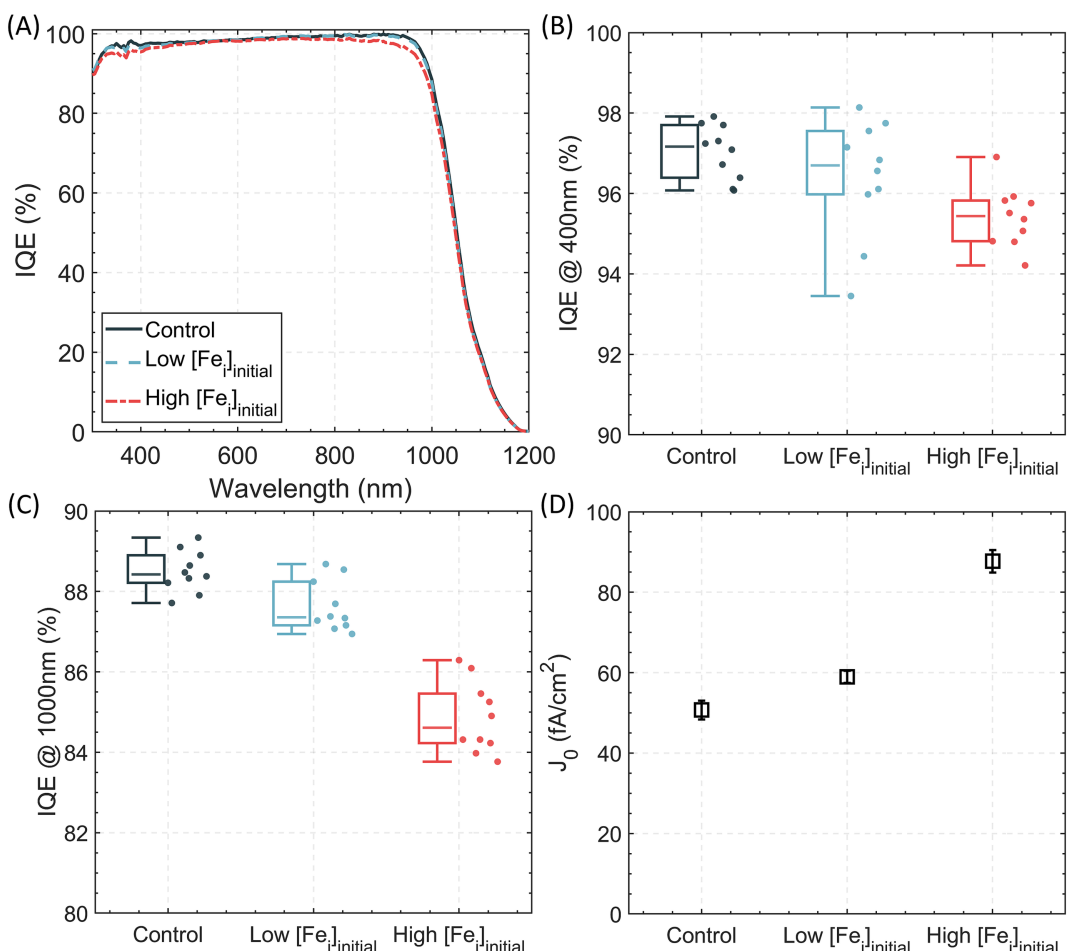


FIGURE 7 | (A) Measured average IQE curves of the n -type front junction poly-Si/SiO_x-based solar cells with no (control), low ($[Fe_i]_{\text{initial}} = 2 \times 10^{12} \text{ cm}^{-3}$), and high ($[Fe_i]_{\text{initial}} = 1 \times 10^{13} \text{ cm}^{-3}$) Fe implantation doses. (B, C) Measured average IQE at a wavelength of 400 and 1000 nm, respectively. (D) Measured double-side surface recombination current density (J_0) of the n -type front junction poly-Si/SiO_x-based solar cells precursors before metallization with different initial bulk Fe concentrations.

Fe concentration around $2 \times 10^{13} \text{ cm}^{-3}$, when the active boron concentration in the *p*-type emitter is below $5 \times 10^{19} \text{ cm}^{-3}$, the accumulated Fe atoms in the *p*-type emitter can significantly degrade the emitter saturation current density (J_{0E}). As shown by the ECV profile in Figure S6, the homogenous *p*-type emitter used in this work has an average active boron concentration of $2 \times 10^{19} \text{ cm}^{-3}$. The exact amount of the gettered Fe concentration in the *p*-type emitter depends on the blocking strength of the SiO_x interlayer [17], the gettering strength of the *n*-type poly-Si layer [18] and the doping profile of the *p*-type emitter itself [64]. Based on the same assumed parameters as used in Section 3.1.1 from our previous gettering studies [17, 18], a high level of Fe accumulation of about $6 \times 10^{13} \text{ cm}^{-3}$ in the *p*-type emitter can be expected from simulation. The Fe concentration in the *p*-type emitter may be even higher if the SiO_x blocking effect is stronger. Hence, it is reasonable to expect an Fe-induced J_{0E} degradation for the *p*-type emitter. On the other hand, *n*-type emitter was found to be unaffected by Fe gettering, as the SRH recombination due to interstitial Fe is not comparable to the strong Auger recombination in the heavily doped *n*-type emitter, unlike the FeB pairs in the *p*-type emitter [20].

Therefore, based on both the IQE results at 400 nm (Figure 7B) and the double-side J_0 results (Figure 7D), we can conclude that the gettered Fe atoms in the *p*-type emitter can increase the emitter recombination rate and degrade the *n*-FJ poly-Si/ SiO_x -based solar cell performance.

On the other hand, the IQE values at a long wavelength of 1000 nm indicate the rear surface recombination and bulk recombination, due to deep absorption of photons of a 1000 nm wavelength. Based on the previous results in Section 3.1.2 that the poly-Si/ SiO_x passivation is not affected by Fe gettering, the IQE variation at 1000 nm for the cells with different initial bulk Fe concentrations can be directly attributed to the different bulk recombination rates.

As previously shown in Figure 3, after the POCl_3 diffusion step, about 99% of the initial bulk Fe concentration is removed from the c-Si bulk. As the *n*-FJ poly-Si/ SiO_x -based solar cells only benefit from the poly-Si/ SiO_x gettering effect on the rear side, a fraction of 2% of the initial bulk Fe concentration is expected to remain in the c-Si bulk after the single side poly-Si/ SiO_x formation (the *p*-type emitter gettering does not affect the bulk Fe concentration largely due to its weak gettering effect). The remaining bulk Fe concentrations of $4 \times 10^{10} \text{ cm}^{-3}$ (for the low $[\text{Fe}]_{\text{initial}}$) and $2 \times 10^{11} \text{ cm}^{-3}$ (high $[\text{Fe}]_{\text{initial}}$) would result in SRH lifetimes of 32.6 and 6.5 ms, respectively, at an injection level of $1 \times 10^{15} \text{ cm}^{-3}$, using the SRH parameters of interstitial Fe from Refs [12, 65]. Taking into account the intrinsic and surface recombination components (as shown in Figure 7D), the effective lifetimes are expected to be 2.5, 2.0, and 1.2 ms, respectively, at an injection level of $1 \times 10^{15} \text{ cm}^{-3}$, for the control cell and the cells with $[\text{Fe}]_{\text{initial}} = 2 \times 10^{12} \text{ cm}^{-3}$ and $1 \times 10^{13} \text{ cm}^{-3}$, which may explain the IQE variation at 1000 nm as observed above.

It is worth noting that the possible difference in the V_{oc} values due to different levels of Fe contamination could be larger than shown here, if better surface passivation were applied. The cells

from this work were largely limited by the front side surface passivation from the AlO_x layers. It was tested that the single-side J_0 value of the samples passivated by the same AlO_x layers is around 20 fA/cm^2 on un-doped planar substrates (compared with the excellent passivation of a J_0 value of around 3 fA/cm^2 on un-doped textured substrates in [4]). The passivation performance of AlO_x layers would be even worse when applied to the *n*-type FJ solar cells featuring a textured surface with *p*-type emitter. This means that the impact of the Fe contamination and gettering could be more noticeable if excellent front-side passivation were applied. Specially, the difference in the V_{oc} values between the control cells and cell with low $[\text{Fe}]_{\text{initial}}$ might be more obvious.

In summary, the results from the current–voltage, IQE and lifetime measurements show that an initially significant Fe contamination ($[\text{Fe}]_{\text{initial}} = 1 \times 10^{13} \text{ cm}^{-3}$) can reduce the V_{oc} and J_{sc} of the *n*-FJ poly-Si/ SiO_x -based solar cells, which most probably can be attributed to the different remaining bulk Fe concentrations and the different emitter saturation current densities due to Fe accumulation.

3.2.2 | Suns- V_{oc} Measurements

In this work, due to series resistance issues, we used the average pseudo-JV curves derived from Suns- V_{oc} measurements to analyze the effect of Fe gettering on pseudo-FF (pFF), as shown in Figure 8A. The Suns- V_{oc} curve was converted to the pseudo-JV curve using a superposition principle [66], with the measured J_{sc} values at 1-Sun illumination. The shunting resistances of the cells were measured and confirmed to be sufficiently high and thus not affecting the cell performance. Figure 8B,C present pFF and pseudo-efficiency (pEff) values derived from the Suns- V_{oc} measurements.

As shown in Figure 8B, the control cells present an average pFF value of 81.6%. As the $[\text{Fe}]_{\text{initial}}$ increases to 2×10^{12} and $1 \times 10^{13} \text{ cm}^{-3}$, the average pFF drops to 81.0% and 80.0%, respectively. However, the reduction in pFF cannot be fully explained by the differences in the V_{oc} values. The ideal fill factor (FF_0) values were extracted from the V_{oc} and J_{sc} values (from Figure 6) with an assumed ideality factor $n=1$, and results show that the FF_0 values vary by less than 0.5% among the cells with different initial bulk Fe concentrations (see Figure S7). Figure 8D shows the fill factor differences between the pseudo fill factors and calculated ideal fill factors ($\Delta\text{FF} = \text{pFF} - \text{FF}_0$), and the absolute difference becomes larger with increasing initial bulk Fe concentrations. Hence, there are other mechanisms leading to the reduction of pFF values or the increasing ideality factors for the cells with higher initial bulk Fe concentrations, and this would degrade the cell performance further. As shown in Figure 8C, the average pEff values reduce from 22.7% to 22.5% and 21.5%, as a result of reduced V_{oc} , J_{sc} , and pFF with increasing $[\text{Fe}]_{\text{initial}}$.

To confirm the pFF trend, Figure S8 shows the ideality factors of the *n*-FJ poly-Si/ SiO_x -based solar cells with different initial bulk Fe concentrations, extracted from the Sun- V_{oc} IV curves and PL imaging at various exposure intensities (0.1–0.8 Sun). The results show an obvious increasing trend of the ideality

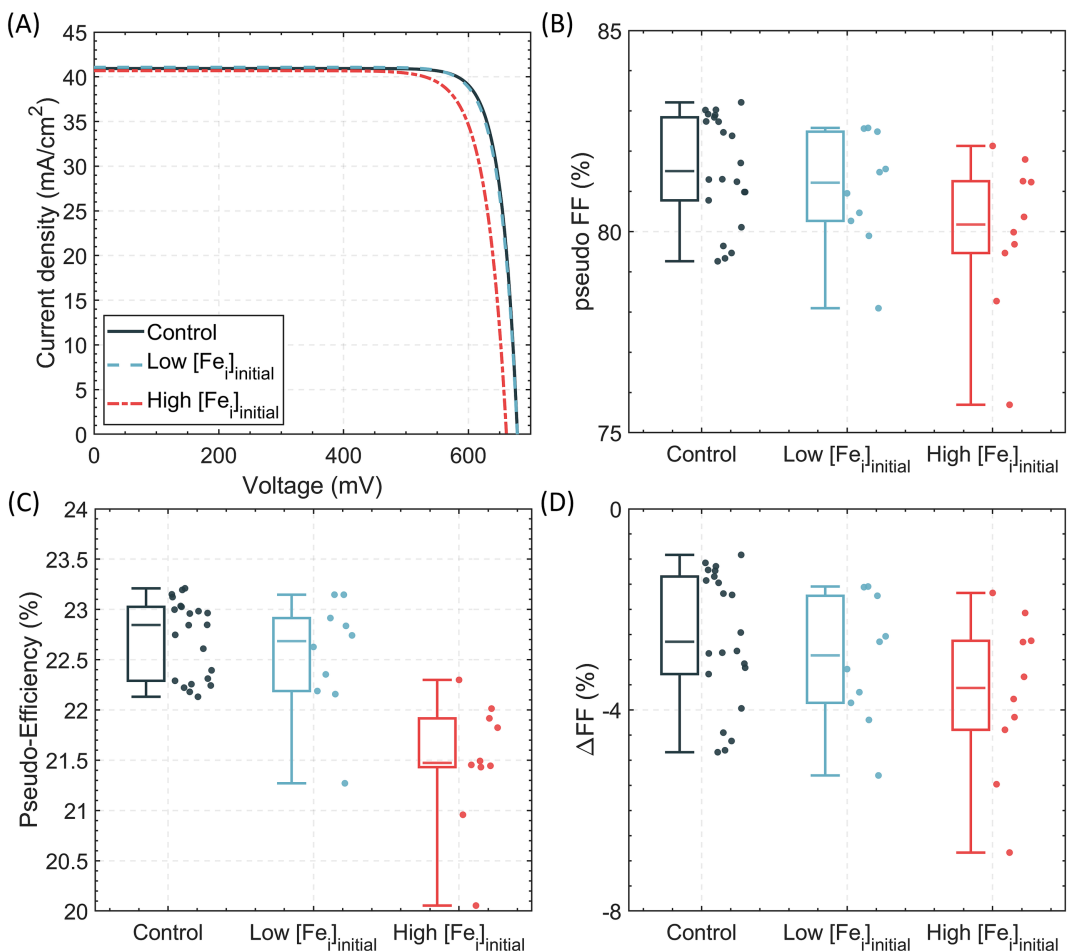


FIGURE 8 | (A) Current density–voltage curves from Suns- V_{oc} measurements of the n -type front junction poly-Si/SiO_x solar cells with no (control), low ($[Fe_i]_{initial} = 2 \times 10^{12} \text{ cm}^{-3}$), and high ($[Fe_i]_{initial} = 1 \times 10^{13} \text{ cm}^{-3}$) Fe implantation doses. (B, C) Calculated pseudo fill factors and efficiencies from the IV curves derived from Suns- V_{oc} measurements. (D) Fill factor difference between the calculated pseudo fill factors and ideal fill factors ($pFF - FF_0$).

factor with increasing initial bulk Fe concentrations, and the results from two different measurement techniques are consistent. Meanwhile, from the mapping in Figure S8B, it is clear that the ideality factor increases uniformly across the whole cell area.

It was reported that the injection dependence of bulk recombination would result in reduced fill factor in p -type c-Si solar cells [67]. Nevertheless, Fe in n -type Si is not expected to demonstrate significant injection dependence [16]. Hence, the remaining bulk Fe in n -type c-Si is commonly considered to affect V_{oc} and J_{sc} values rather than the fill factors. A recent study reported that the n -type melt-recharged CZ c-Si wafers with different metal impurities in the feedstock exhibit obvious FF reductions but similar V_{oc} and J_{sc} values [68]. However, there are other recombination centers in the bulk (e.g., oxide precipitates) in that study [68], making it difficult to make a direct comparison to our study.

To understand the reason for the observed pFF reduction (or ideality factor increase) with increasing initial bulk Fe concentrations, firstly, we utilized lock-in thermography (LIT) and high-resolution PL imaging to look for local defects in the cells. It was reported that local non-ideal shunting or recombination may cause an increase of local ideality factor and thus a reduction of fill factor [69]. However, we did not observe any local

shunting or recombination spots in the cell area and therefore we rule out the contribution of local defects.

Secondly, although the n -type cells with bulk Fe contamination are not expected to show injection dependent bulk lifetimes, the front surface recombination may be injection dependent due to Fe-induced recombination in the p -type emitter. Therefore, we measured the photoluminescence quenching efficiency (PLQE) to extract the carrier collection efficiency at various suns intensities [70], and the results show that the PLQE of the cells with Fe contamination only exhibit minor injection dependence. Besides, in the emitter region, low injection condition is normally assumed, and this injection dependence is negligible at low injections. Therefore, the slight injection dependence cannot fully explain the pFF reduction.

Lastly, recombination in the space charge region is considered, where recombination rate is limited by both the majority and minority carrier concentrations, and this can reduce the fill factor of the solar cell [71]. In this work, the reduction of pFF is suspected to come from the space charge region recombination due to Fe-induced traps in the space charge region. Nevertheless, it needs further investigation to understand whether or not Fe could affect the recombination in the space charge region and what the underlying mechanism would be.

3.2.3 | Temperature Coefficient

The TC is a critical parameter for accurately evaluating the c-Si solar cell performance at various operating temperatures, which is important for predicting energy output from PV systems. Figure 9A shows the measured TC (V_{oc}) values of the *n*-FJ poly-Si/SiO_x-based solar cells with different initial bulk Fe concentrations at one-sun illumination and in the range of 298–323 K. The control cells present TC values of around $-1.82 \text{ mV}^\circ\text{C}$, which is similar to the temperature sensitivity of poly-Si/SiO_x-based solar cells reported in [72]. As the initial bulk Fe concentration increases, there is a clear increase of the absolute TC values. The results suggest that, besides the reduction of V_{oc} , J_{sc}, and FF, the presence of Fe in the initial c-Si bulk would make the poly-Si/SiO_x-based solar cell efficiency more sensitive to temperature increases.

To understand the impact of Fe contamination on the temperature sensitivity, Figure 9B presents the calculated γ values of the cells with different initial bulk Fe concentrations based on the measured TC (V_{oc}), as the TC (V_{oc}) values present an approximately linear relationship with the V_{oc} values of the cell [73]:

$$TC(V_{oc}) = \frac{dV_{oc}}{dT} = -\frac{\frac{E_{g0}}{q} - V_{oc} + \frac{\gamma k_B T}{q}}{T} \quad (1)$$

where E_{g0} is the semiconductor bandgap energy extrapolated at 0 K (1.12 eV for Si); q is the elementary charge ($1.6 \times 10^{-19} \text{ C}$); k_B is the Boltzmann constant (8.617 eV/K); T is the solar cell temperature in Kelvin; and γ represents the temperature dependence of the dark saturation current density J_0 depending on the dominant recombination mechanism.

The results show an increasing trend in γ values with increasing initial bulk Fe concentrations, which indicates different temperature dependencies of the dominant recombination mechanism within the cells. An increasing γ value is reported to correlate with increasing ideality factor [74] and an additional gettering step can relieve γ values [75]. Hence, it is likely that the temperature sensitivity is related to the observed changes in pFF as discussed above in Section 3.2.2.

4 | Discussion

Overall, we have demonstrated that the poly-Si/SiO_x passivation effect is not affected by Fe gettering, but the initial Fe contamination in the c-Si bulk, if significant (e.g., $[Fe_i]_{\text{initial}} = 1 \times 10^{13} \text{ cm}^{-3}$), would deteriorate the *n*-FJ poly-Si/SiO_x-based solar cells performance in terms of voltage, current, fill factor, and TC. Note that the silicon wafers with $[Fe_i]_{\text{initial}} = 1 \times 10^{13} \text{ cm}^{-3}$ and $[Fe_i]_{\text{initial}} = 2 \times 10^{12} \text{ cm}^{-3}$ represent the multi-crystalline (top and bottom parts of the ingot) and CZ-Si (tail region of the ingot) wafers, respectively. The CZ-Si wafers in the middle region of the ingot are expected to have much lower Fe content than the wafers examined in this work [32, 51].

Nevertheless, there are two observations that need attention: (1) The gettered Fe in the *p*-type emitter is shown to degrade the front surface passivation; (2) a significant initial bulk Fe contamination causes a reduction in fill factor and TC. The increased recombination rate of the *p*-type emitter due to Fe contamination can be explained by the contribution of SRH recombination in the *p*-type lightly doped emitter, while it needs further investigation to understand how Fe gettering would affect the FF and TC values.

The impact of Fe gettering on the *p*-type emitter recombination can be more significant than the results shown in Figure 7, if the poly-Si/SiO_x-based solar cells feature selective emitters and excellent surface passivation on the front side. In a selective emitter cell, the shallow *p*-type emitters between fingers are generally lightly doped to achieve good passivation (e.g., $300 \Omega/\text{sq}$ in [4]), in which case the emitter recombination rate would be more strongly affected by SRH recombination in the diffused region [20, 30]. In addition, localized, heavily doped selective emitters means that a more sophisticated three-dimensional gettering model is needed to simulate the non-uniform Fe distribution during the cell fabrication process, which has implications for the emitter recombination rate.

The *n*-type FJ poly-Si/SiO_x-based solar cells in this work follow similar fabrication process as commonly applied in industry (except metallization), as shown in Figure 2. Although the deposition and diffusion temperature profiles may vary slightly due to different equipment optimization, the findings in this work can

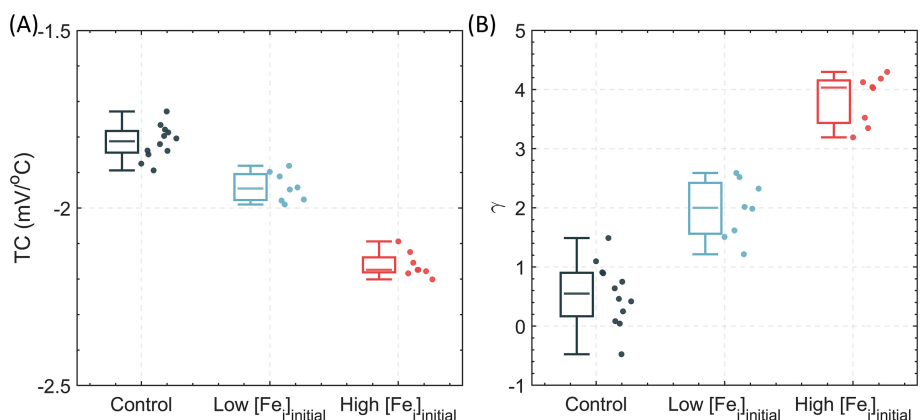


FIGURE 9 | (A) Measured temperature coefficients of open-circuit voltage and (B) calculated γ values for the *n*-type front junction poly-Si/SiO_x solar cells with no (control), low ($[Fe_i]_{\text{initial}} = 2 \times 10^{12} \text{ cm}^{-3}$), and high ($[Fe_i]_{\text{initial}} = 1 \times 10^{13} \text{ cm}^{-3}$) Fe implantation doses, at one-sun illumination and in the range of 298–323 K.

provide a good indication for industrial solar cells. However, it is worth noting that the cells fabricated in this work went through an FGA process rather than the commonly used firing process in the industry. The low temperature FGA enhances the overall gettering effectiveness, reducing the remaining bulk Fe concentration but at the same time leading to a slightly higher Fe concentration in the *p*-type emitter (based on diffusion limited segregation gettering model [19, 64]). This may be preferred if the wafers contain a high-level of metal contamination, in which case the overall solar cell performance is limited by the c-Si bulk quality. On the other hand, the firing process may compromise the overall gettering effectiveness due to the redistribution of metal impurities, which may not be an issue for high-quality wafers. However, the metal contamination may not only come from the original wafer bulk but also from the fabrication process, which may happen during the high temperature firing process, as demonstrated by the simulated firing process in this study (Section 3.1.1). The change of bulk Fe concentration during the FGA or firing process depends on both the gettering strength and kinetics of the poly-Si/SiO_x passivating contact. If the blocking effect from the SiO_x interlayer is weak, the remaining bulk Fe concentration can be much higher after the firing process. Therefore, a subsequent low temperature anneal can be applied to enhance the gettering effectiveness, while the degradation of *p*-type emitter needs to be considered at the same time.

5 | Conclusion

In this work, we assessed the impact of bulk Fe contamination and gettering on the poly-Si/SiO_x passivation quality and the resulting solar cell performance. We found that the gettering of Fe during the poly-Si/SiO_x fabrication process would not affect its passivation quality, for both *n*-type phosphorus-doped and *p*-type boron-doped poly-Si/SiO_x. Meanwhile, we did not observe any significant impact of the gettered Fe on the hydrogenation response (firing stability) of poly-Si/SiO_x. However, a significant concentration of bulk Fe impurities ($1 \times 10^{13} \text{ cm}^{-3}$) can degrade the *n*-FJ poly-Si/SiO_x-based solar cell performance in terms of V_{oc}, J_{sc}, FF, and TC (V_{oc}). The accumulation of the gettered Fe in the *p*-type lightly doped emitter is found to be detrimental to the front side emitter passivation. Together with the remaining Fe contamination in the c-Si bulk, they can result in a reduction in both V_{oc} and J_{sc}, as revealed by the lifetime and QE measurements. A reduction in FF and TC (V_{oc}) is also observed, and this is suspected to be caused by an increased space charge region recombination due to Fe traps, while the underlying reason needs further investigation. Nevertheless, for an initial bulk Fe concentration of $2 \times 10^{12} \text{ cm}^{-3}$, which should be much higher than the Fe content in the current CZ-Si wafers, the impact of bulk Fe and Fe gettering on cell performance is found to be small.

Acknowledgments

This work has been supported by the Australian Renewable Energy Agency (ARENA) through the Australian Centre for Advanced Photovoltaics (ACAP), project 2022/TRAC004. We acknowledge access to NCRIS-funded facilities and expertise at the ion-implantation Laboratory (iiLab), a node of the Heavy Ion Accelerator (HIA) Capability at the Australian National University Reference. This work has been

made possible through the access to the ACT node of the Australian National Fabrication Facility (ANFF-ACT).

Data Availability Statement

The data that support the findings of this study are available from the corresponding author upon reasonable request.

References

1. "Fraunhofer Institute for Solar Energy Systems ISE: Fraunhofer Institute for Solar Energy Systems," Photovoltaics Report, 2023. [Online], <https://www.ise.fraunhofer.de/en/publications/studies/photovoltaics-report.html>.
2. F. Haase, C. Hollemani, S. Schäfer, et al., "Laser Contact Openings for Local Poly-Si-Metal Contacts Enabling 26.1%-Efficient POLO-IBC Solar Cells," *Solar Energy Materials & Solar Cells* 186, no. June (2018): 184–193, <https://doi.org/10.1016/j.solmat.2018.06.020>.
3. P. Zheng, J. Yang, Z. Wang, et al., "Detailed Loss Analysis of 24.8% Large-Area Screen-Printed *n*-Type Solar Cell With Polysilicon Passivating Contact," *Cell Reports Physical Science* 2, no. 10 (2021): 100603, <https://doi.org/10.1016/j.xrpp.2021.100603>.
4. A. Richter, R. Müller, J. Benick, et al., "Design Rules for High-Efficiency Both-Sides-Contacted Silicon Solar Cells With Balanced Charge Carrier Transport and Recombination Losses," *Nature Energy* 6, no. 4 (2021): 429–438, <https://doi.org/10.1038/s41560-021-00805-w>.
5. C. Messmer, A. Fell, F. Feldmann, N. Wöhrle, J. Schön, and M. Hermle, "Efficiency Roadmap for Evolutionary Upgrades of PERC Solar Cells by TOPCon: Impact of Parasitic Absorption," *IEEE Journal of Photovoltaics* 10, no. 2 (2020): 335–342, <https://doi.org/10.1109/JPHOTOV.2019.2957642>.
6. D. Yan, A. Cuevas, J. I. Michel, et al., "Polysilicon Passivated Junctions: The Next Technology for Silicon Solar Cells?," *Joule* 5, no. 4 (2021): 811–828, <https://doi.org/10.1016/j.joule.2021.02.013>.
7. J. Krügener, F. Haase, M. Rienäcker, R. Brendel, H. J. Osten, and R. Peibst, "Improvement of the SRH Bulk Lifetime Upon Formation of *n*-Type POLO Junctions for 25% Efficient Si Solar Cells," *Solar Energy Materials & Solar Cells* 173, no. April (2017): 85–91, <https://doi.org/10.1016/j.solmat.2017.05.055>.
8. A. Liu, D. Yan, S. P. Phang, A. Cuevas, and D. Macdonald, "Effective Impurity Gettering by Phosphorus- and Boron-Diffused Polysilicon Passivating Contacts for Silicon Solar Cells," *Solar Energy Materials & Solar Cells* 179, no. September 2017 (2018): 136–141, <https://doi.org/10.1016/j.solmat.2017.11.004>.
9. M. Hayes, B. Martel, G. W. Alam, et al., "Impurity Gettering by Boron- and Phosphorus-Doped Polysilicon Passivating Contacts for High-Efficiency Multicrystalline Silicon Solar Cells," *Physica Status Solidi A: Applications and Materials Science* 216, no. 17 (2019): 1900321, <https://doi.org/10.1002/pssa.201900321>.
10. Z. Wang, Z. Liu, M. Liao, et al., "Effective Gettering of In-Situ Phosphorus-Doped Polysilicon Passivating Contact Prepared Using Plasma-Enhanced Chemical-Vapor Deposition Technique," *Solar Energy Materials & Solar Cells* 206, no. August 2019 (2020): 110256, <https://doi.org/10.1016/j.solmat.2019.110256>.
11. E. R. Weber, "Transition Metals in Silicon," *Applied Physics A: Materials Science & Processing* 30, no. 1 (1983): 1–22, <https://doi.org/10.1007/BF00617708>.
12. A. A. Istratov, H. Hieslmair, and E. R. Weber, "Iron and Its Complexes in Silicon," *Applied Physics A: Materials Science & Processing* 69, no. 1 (1999): 13–44, <https://doi.org/10.1007/s003390050968>.
13. K. Graff, *Metal Impurities in Silicon-Device Fabrication* (Berlin, Heidelberg: Springer Berlin Heidelberg, 2001).

14. W. Shockley and W. T. Read, "Statistics of the Recombinations of Holes and Electrons," *Physics Review* 87, no. 5 (1952): 835–842, <https://doi.org/10.1103/PhysRev.87.835>.
15. R. Hall, "Germanium Rectifier Characteristics," *Physics Review* 83, no. 1 (1951): 228.
16. D. Macdonald and L. J. Geerligs, "Recombination Activity of Interstitial Iron and Other Transition Metal Point Defects in p- and n-Type Crystalline Silicon," *Applied Physics Letters* 85, no. 18 (2004): 4061–4063, <https://doi.org/10.1063/1.1812833>.
17. Z. Yang, J. Krügener, F. Feldmann, et al., "Impurity Gettering in Polycrystalline-Silicon Based Passivating Contacts—The Role of Oxide Stoichiometry and Pinholes," *Advanced Energy Materials* 12 (2022): 1–11, <https://doi.org/10.1002/aenm.202103773>.
18. Z. Yang, J. Krügener, F. Feldmann, et al., "Comparing the Gettering Effect of Heavily Doped Polysilicon Films and Its Implications for Tunnel Oxide-Passivated Contact Solar Cells," *Solar RRL* 7 (2022): 2200578, <https://doi.org/10.1002/solr.202200578>.
19. A. Liu, Z. Yang, F. Feldmann, et al., "Understanding the Impurity Gettering Effect of Polysilicon/Oxide Passivating Contact Structures Through Experiment and Simulation," *Solar Energy Materials & Solar Cells* 230, no. June (2021): 111254, <https://doi.org/10.1016/j.solmat.2021.111254>.
20. D. Macdonald, H. Mäckel, and A. Cuevas, "Effect of Gettered Iron on Recombination in Diffused Regions of Crystalline Silicon Wafers," *Applied Physics Letters* 88, no. 9 (2006): 1–4, <https://doi.org/10.1063/1.2181199>.
21. D. L. Young, W. Nemeth, V. LaSalvia, et al., "Interdigitated Back Passivated Contact (IBPC) Solar Cells Formed by Ion Implantation," *IEEE Journal of Photovoltaics* 6, no. 1 (2016): 41–47, <https://doi.org/10.1109/JPHOTOV.2015.2483364>.
22. F. Feldmann, J. Schön, J. Niess, W. Lerch, and M. Hermle, "Studying Dopant Diffusion From Poly-Si Passivating Contacts," *Solar Energy Materials & Solar Cells* 200, no. April (2019): 109978, <https://doi.org/10.1016/j.solmat.2019.109978>.
23. O. Kononchuk, K. G. Koralev, N. Yarykin, and G. A. Rozgonyi, "Diffusion of Iron in the Silicon Dioxide Layer of Silicon-on-Insulator Structures," *Applied Physics Letters* 73, no. 9 (1998): 1206–1208, <https://doi.org/10.1063/1.122128>.
24. J. Leveneur, M. Langlois, J. Kennedy, and J. B. Metson, "Excess Oxygen Limited Diffusion and Precipitation of Iron in Amorphous Silicon Dioxide," *Journal of Applied Physics* 122, no. 13 (2017): 135302, <https://doi.org/10.1063/1.4985819>.
25. G. Coletti, P. C. P. Bronsveld, G. Hahn, et al., "Impact of Metal Contamination in Silicon Solar Cells," *Advanced Functional Materials* 21, no. 5 (2011): 879–890, <https://doi.org/10.1002/adfm.201000849>.
26. J. Schmidt, B. Lim, D. Walter, et al., "Impurity-Related Limitations of Next-Generation Industrial Silicon Solar Cells," *IEEE Journal of Photovoltaics* 3, no. 1 (2013): 114–118, <https://doi.org/10.1109/JPHOTOV.2012.2210030>.
27. V. Vähänissi, A. Haarahiltunen, H. Talvitie, M. Yli-Koski, and H. Savin, "Impact of Phosphorus Gettering Parameters and Initial Iron Level on Silicon Solar Cell Properties," *Progress in Photovoltaics: Research and Applications* 21 (2013): 1127–1135, <https://doi.org/10.1002/pip.2215>.
28. A. Richter, J. Benick, F. Feldmann, A. Fell, M. Hermle, and S. W. Glunz, "n-Type Si Solar Cells With Passivating Electron Contact: Identifying Sources for Efficiency Limitations by Wafer Thickness and Resistivity Variation," *Solar Energy Materials & Solar Cells* 173 (2017): 96–105, <https://doi.org/10.1016/j.solmat.2017.05.042>.
29. A. Richter, J. Benick, A. Fell, M. Hermle, and S. W. Glunz, "Impact of Bulk Impurity Contamination on the Performance of High-Efficiency n-Type Silicon Solar Cells," *Progress in Photovoltaics*: Research and Applications 26, no. 5 (2018): 342–350, <https://doi.org/10.1002/pip.2990>.
30. T. Weber, C. Zechner, D. Macdonald, and P. P. Altermatt, "Numerical Simulation of Gettering and Recombination in Iron-Contaminated Boron Emitters," in *Proc. 21st European PV Solar Energy Conf. (EU PVSEC)* (2006): 1486–1489.
31. D. Macdonald, T. Roth, P. N. K. Deenapanray, T. Trupke, and R. A. Bardos, "Doping Dependence of the Carrier Lifetime Crossover Point Upon Dissociation of Iron-Boron Pairs in Crystalline Silicon," *Applied Physics Letters* 89, no. 14 (2006): 2004–2007, <https://doi.org/10.1063/1.2358126>.
32. T. Le, Y. Cai, Z. Yang, R. Chen, D. Macdonald, and A. Liu, "Industrial Czochralski-Grown n-Type Silicon Wafers: Gettering Effectiveness and Possible Bulk Limiting Defects," *Solar RRL* 8 (2023): 2300928.
33. J. Hofstetter, D. P. Fenning, D. M. Powell, A. E. Morishige, and T. Buonassisi, "Iron Management in Multicrystalline Silicon Through Predictive Simulation: Point Defects, Precipitates, and Structural Defect Interactions," *Solid State Phenomena* 205–206 (2014): 15–25, <https://doi.org/10.4028/www.scientific.net/SSP.205-206.15>.
34. D. Macdonald, P. N. K. Deenapanray, and S. Diez, "Onset of Implant-Related Recombination in Self-Ion Implanted and Annealed Crystalline Silicon," *Journal of Applied Physics* 96, no. 7 (2004): 3687–3691, <https://doi.org/10.1063/1.1789630>.
35. J. Stuckelberger, D. Yan, S. P. Phang, et al., "Pre-Annealing for Improved LPCVD Deposited Boron-Doped Poly-Si Hole-Selective Contacts," *Solar Energy Materials and Solar Cells* 251, no. December 2022 (2023): 112123, <https://doi.org/10.1016/j.solmat.2022.112123>.
36. G. Zoth and W. Bergholz, "A Fast, Preparation-Free Method to Detect Iron in Silicon," *Journal of Applied Physics* 67, no. 11 (1990): 6764–6771, <https://doi.org/10.1063/1.345063>.
37. D. H. Macdonald, L. J. Geerligs, and A. Azzizi, "Iron Detection in Crystalline Silicon by Carrier Lifetime Measurements for Arbitrary Injection and Doping," *Journal of Applied Physics* 95, no. 3 (2004): 1021–1028, <https://doi.org/10.1063/1.1637136>.
38. R. A. Sinton and A. Cuevas, "Contactless Determination of Current-Voltage Characteristics and Minority-Carrier Lifetimes in Semiconductors From Quasi-Steady-State Photoconductance Data," *Applied Physics Letters* 69, no. 17 (1996): 2510–2512, <https://doi.org/10.1063/1.117723>.
39. T. T. Le, S. P. Phang, Z. Yang, D. Macdonald, and A. Liu, "Impact of Depth-Wise Inhomogeneous Iron Distributions on the Accuracy of Lifetime-Based Interstitial Iron Measurements on Silicon Wafers," *IEEE Journal of Photovoltaics* 13, no. 4 (2023): 495–502, <https://doi.org/10.1109/JPHOTOV.2023.3261549>.
40. D. E. Kane and R. M. Swanson, "Measurement of the Emitter Saturation Current by a Contactless Photoconductivity Decay Method," in *Conference Record of the IEEE Photovoltaic Specialists Conference* (1985): 578–583.
41. A. Schenk, "Finite-Temperature Full Random-Phase Approximation Model of Band Gap Narrowing for Silicon Device Simulation," *Journal of Applied Physics* 84, no. 7 (1998): 3684–3695, <https://doi.org/10.1063/1.368545>.
42. A. Fell, T. Niewelt, B. Steinhauser, F. D. Heinz, M. C. Schubert, and S. W. Glunz, "Radiative Recombination in Silicon Photovoltaics: Modeling the Influence of Charge Carrier Densities and Photon Recycling," *Solar Energy Materials & Solar Cells* 230, no. June (2021): 111198, <https://doi.org/10.1016/j.solmat.2021.111198>.
43. T. Niewelt, B. Steinhauser, A. Richter, et al., "Reassessment of the Intrinsic Bulk Recombination in Crystalline Silicon," *Solar Energy Materials & Solar Cells* 235 (2022): 111467, <https://doi.org/10.1016/j.solmat.2021.111467>.
44. A. K. Singh, *Advanced X-Ray Techniques in Research and Industry* (Amsterdam, The Netherlands: IOS Press, 2005).

45. A. Liu, S. P. Phang, and D. Macdonald, "Gettering in Silicon Photovoltaics: A Review," *Solar Energy Materials & Solar Cells* 234 (2022): 111447, <https://doi.org/10.1016/j.solmat.2021.111447>.
46. S. P. Phang and D. MacDonald, "Direct Comparison of Boron, Phosphorus, and Aluminum Gettering of Iron in Crystalline Silicon," *Journal of Applied Physics* 109, no. 7 (2011): 1100031–1100036, <https://doi.org/10.1063/1.3569890>.
47. C. Fischer, A. Zuschlag, and G. Hahn, "Various Impacts of Firing Temperature on Crystalline Silicon," *AIP Conference Proceedings* 2826, no. 1 (2023): 110003, <https://doi.org/10.1063/5.0143430>.
48. J. I. Polzin, S. Lange, S. Richter, et al., "Temperature-Induced Stoichiometric Changes in Thermally Grown Interfacial Oxide in Tunnel-Oxide Passivating Contacts," *Solar Energy Materials & Solar Cells* 218, no. July (2020): 110713, <https://doi.org/10.1016/j.solmat.2020.110713>.
49. R. Basnet, D. Yan, D. Kang, et al., "Current Status and Challenges for Hole-Selective Poly-Silicon Based Passivating Contacts," *Applied Physics Reviews* 11, no. 1 (2024): 011311, <https://doi.org/10.1063/5.0185379>.
50. G. Yang, R. Gram, P. Procel, et al., "Will SiO_x-Pinholes for SiO_x/Poly-Si Passivating Contact Enhance the Passivation Quality?," *Solar Energy Materials & Solar Cells* 252, no. January (2023): 112200, <https://doi.org/10.1016/j.solmat.2023.112200>.
51. R. Basnet, C. Sun, T. le, et al., "Investigating Wafer Quality in Industrial Czochralski-Grown Gallium-Doped p-Type Silicon Ingots With Melt Recharging," *Solar RRL* 7, no. 15 (2023): 1–7, <https://doi.org/10.1002/solr.202300304>.
52. D. Van Gestel, I. Gordon, and J. Poortmans, "Metal Induced Crystallization of Amorphous Silicon for Photovoltaic Solar Cells," *Physics Procedia* 11 (2011): 196–199, <https://doi.org/10.1016/j.phpro.2011.01.003>.
53. R. Sharma, J. Szlufcik, and H. Sivaramakrishnan, "p-Type Poly-Si/SiO_x Contact by Aluminum-Induced Crystallization of Amorphous Silicon," *Solar Energy Materials & Solar Cells* 234 (2022): 111416.
54. M. Schnabel, B. W. H. van de Loo, W. Nemeth, et al., "Hydrogen Passivation of Poly-Si/SiO_x Contacts for Si Solar Cells Using Al₂O₃ Studied With Deuterium," *Applied Physics Letters* 112, no. 20 (2018): 203901, <https://doi.org/10.1063/1.5031118>.
55. B. Steinhauser, F. Feldmann, D. Ourinson, H. Nagel, T. Fellmeth, and M. Hermle, "On the Influence of the SiNx Composition on the Firing Stability of Poly-Si/SiNx Stacks," *Physica Status Solidi A: Applications and Materials Science* 217, no. 21 (2020): 2000333, <https://doi.org/10.1002/pssa.202000333>.
56. M. Stöhr, J. Aprojanz, R. Brendel, and T. Dullweber, "Firing-Stable PECVD SiO_xNy/n-Poly-Si Surface Passivation for Silicon Solar Cells," *ACS Applied Energy Materials* 4, no. 5 (2021): 4646–4653, <https://doi.org/10.1021/acsaem.1c00265>.
57. D. Kang, H. C. Sio, J. Stuckelberger, et al., "Optimum Hydrogen Injection in Phosphorus-Doped Polysilicon Passivating Contacts," *ACS Applied Materials & Interfaces* 13, no. 46 (2021): 55164–55171, <https://doi.org/10.1021/acsmami.1c17342>.
58. J. I. Polzin, F. Feldmann, B. Steinhauser, M. Bivour, and M. Hermle, "Annealing and Firing Stability of In Situ Boron-Doped Poly-Si Passivating Contacts," in *AIP Conference Proceedings* (American Institute of Physics Inc., 2023), <https://doi.org/10.1063/5.0143580>.
59. C. Madumelu, Y. Cai, C. Hollemann, et al., "Assessing the Stability of p+ and n+ Polysilicon Passivating Contacts With Various Capping Layers on p-Type Wafers," *Solar Energy Materials & Solar Cells* 253 (2023): 112245, <https://doi.org/10.1016/j.solmat.2023.112245>.
60. A. Liu, C. Sun, V. P. Markevich, A. R. Peaker, J. D. Murphy, and D. Macdonald, "Gettering of Interstitial Iron in Silicon by Plasma-Enhanced Chemical Vapour Deposited Silicon Nitride Films," *Journal of Applied Physics* 120, no. 19 (2016): 193103, <https://doi.org/10.1063/1.4967914>.
61. A. Liu and D. Macdonald, "Impurity Gettering by Atomic-Layer-Deposited Aluminium Oxide Films on Silicon at Contact Firing Temperatures," *Physica Status Solidi RRL: Rapid Research Letters* 12, no. 3 (2018): 1–5, <https://doi.org/10.1002/pssr.201700430>.
62. P. Santos, J. Coutinho, and S. Öberg, "First-Principles Calculations of Iron-Hydrogen Reactions in Silicon," *Journal of Applied Physics* 123, no. 24 (2018): 245703, <https://doi.org/10.1063/1.5039647>.
63. T. N. Truong, D. Yan, W. Chen, et al., "Hydrogenation Mechanisms of Poly-Si/SiO_x Passivating Contacts by Different Capping Layers," *Solar RRL* 4, no. 3 (2020): 1–6, <https://doi.org/10.1002/solr.201900476>.
64. S. A. McHugo, R. J. McDonald, A. R. Smith, D. L. Hurley, and E. R. Weber, "Iron Solubility in Highly Boron-Doped Silicon," *Applied Physics Letters* 73, no. 10 (1998): 1424–1426, <https://doi.org/10.1063/1.121964>.
65. D. Macdonald, J. Tan, and T. Trupke, "Imaging Interstitial Iron Concentrations in Boron-Doped Crystalline Silicon Using Photoluminescence," *Journal of Applied Physics* 103, no. 7 (2008): 1–8, <https://doi.org/10.1063/1.2903895>.
66. R. A. Sinton and A. Cuevas, "A Quasi-Steady-State Open-Circuit Voltage Method for Solar Cell Characterization," in *16th European Photovoltaic Solar Energy Conference* (2000): 1–4.
67. D. Macdonald and A. Cuevas, "Reduced Fill Factors in Multicrystalline Silicon Solar Cells due to Injection Level Dependent Bulk Recombination Lifetimes," *Progress in Photovoltaics: Research and Applications* 8 (2000): 363–375.
68. Z. Hu, M. Cong, X. Zhang, et al., "Effect of Metal Impurities Concentration on Electrical Properties in n-Type Recharged-Czochralski Silicon," *Solar Energy Materials & Solar Cells* 260, no. 2 (2023): 112482, <https://doi.org/10.1016/j.solmat.2023.112482>.
69. O. Breitenstein, P. Altermatt, K. Ramspeck, M. A. Green, J. Zhao, and A. Schenk, "Interpretation of the Commonly Observed I-V Characteristics of c-Si Cells Having Ideality Factor Larger Than Two," Conference Record of the 2006 IEEE 4th World Conference on Photovoltaic Energy Conversion, WCPEC-4, vol. 1, (2006): 879–884.
70. V. Campanari, F. Martelli, A. Agresti, et al., "Reevaluation of Photoluminescence Intensity as an Indicator of Efficiency in Perovskite Solar Cells," *Solar RRL* 6, no. 8 (2022): 2200049, <https://doi.org/10.1002/solr.202200049>.
71. P. P. Altermatt, A. G. Aberle, J. Zhao, A. Wang, and G. Heiser, "A Numerical Model of p-n Junctions Bordering on Surfaces," *Solar Energy Materials & Solar Cells* 74, no. 1–4 (2002): 165–174, [https://doi.org/10.1016/S0927-0248\(02\)00061-2](https://doi.org/10.1016/S0927-0248(02)00061-2).
72. R. Le AH, Basnet, D. Yan, W. Chen, et al., "Temperature-Dependent Performance of Silicon Solar Cells With Polysilicon Passivating Contacts," *Solar Energy Materials & Solar Cells* 225, no. October 2020 (2021): 111020, <https://doi.org/10.1016/j.solmat.2021.111020>.
73. M. A. Green, "General Temperature Dependence of Solar Cell Performance and Implications for Device Modelling," *Progress in Photovoltaics: Research and Applications* 11, no. 5 (2003): 333–340, <https://doi.org/10.1002/pip.496>.
74. O. Dupré, R. Vaillon, and M. A. Green, "Thermal Behavior of Photovoltaic Devices," (2017), <https://doi.org/10.1007/978-3-319-49457-9>.
75. S. Nie, R. L. Chin, A. M. Soufiani, et al., "Temperature Sensitivity Maps of Silicon Wafers From Photoluminescence Imaging: The Effect of Gettering and Hydrogenation," *Progress in Photovoltaics: Research and Applications* 30, no. 11 (2022): 1298–1311, <https://doi.org/10.1002/pip.3579>.

Supporting Information

Additional supporting information can be found online in the Supporting Information section.

[Supporting information]

Effect of iron contamination and polysilicon gettering on the performance of polysilicon-based passivating contact solar cells

Zhongshu Yang^{a*}, Rabin Basnet^a, Chris Samundsett^a, Sieu Pheng Phang^a, Thien Truong^{a,b}, Di Kang^a, Wensheng Liang^a, Anh Dinh Bui^a, Wei Wang^a, Tien T. Le^a, Daniel Macdonald^a, AnYao Liu^{a*}

^aSchool of Engineering, The Australian National University, Canberra, Australian Capital Territory, Australia

^bNational Renewable Energy Laboratory, Golden, CO 80401, USA.

*E-mail: zhongshu.yang@anu.edu.au; anyao.liu@anu.edu.au

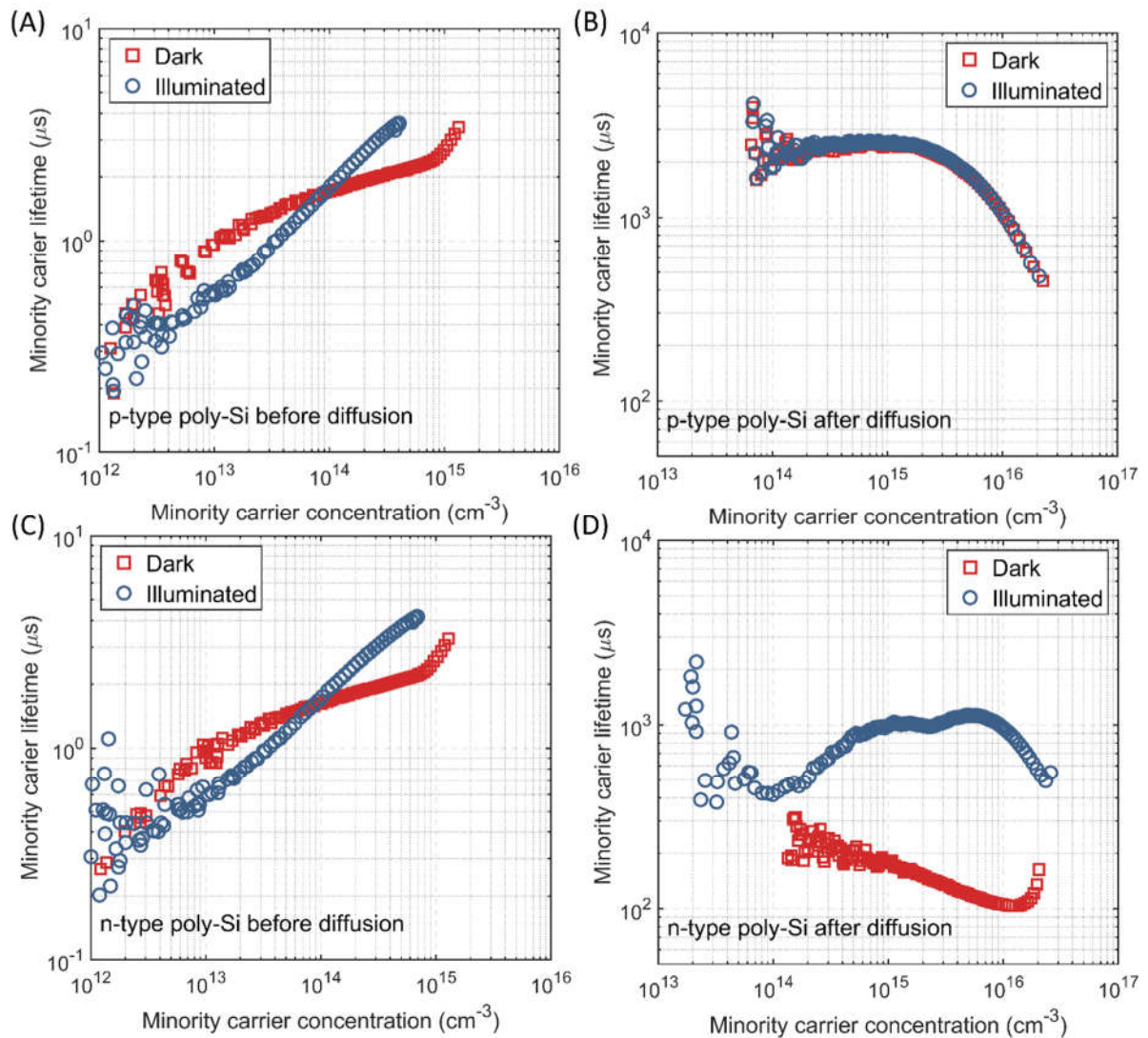


Figure S1. Measured injection dependent carrier lifetimes of the samples passivated by p-type or n-type poly-Si/SiO_x before and diffusion, in the dark and illuminated states. The lifetimes in the two states can be used to estimate the bulk Fe concentration. Note that the lifetime scales are different before and after diffusion, as the lifetimes are much lower before diffusion due to both high bulk recombination from Fe and high surface recombination prior to poly-Si/SiO_x diffusion and formation.

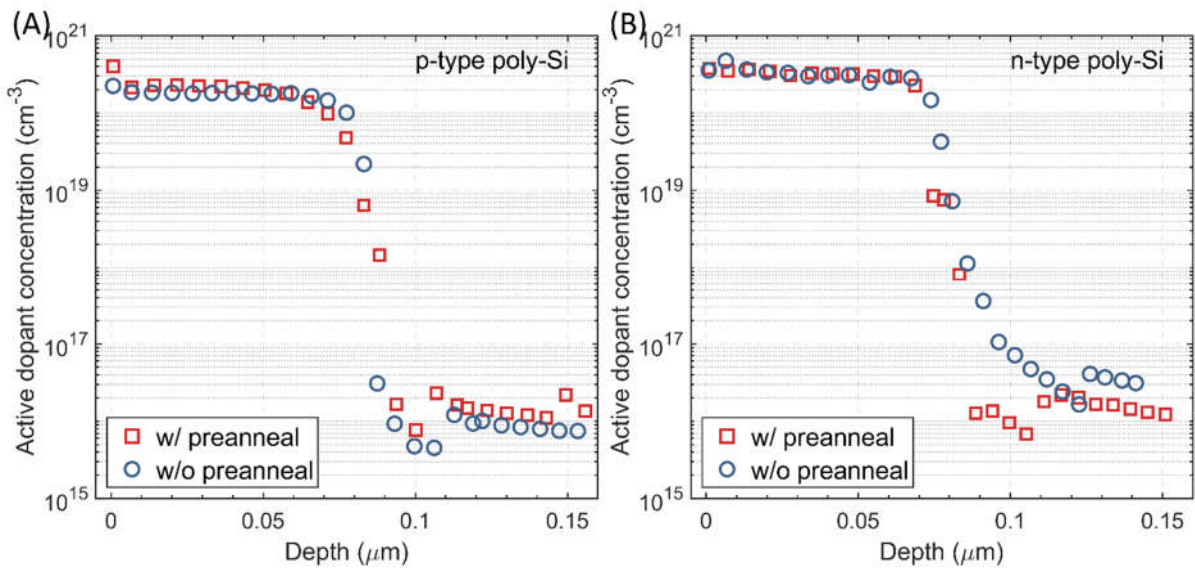


Figure S2. Measured active dopant profiles of boron and phosphorus doped poly-Si/SiO_x structures with or without pre-annealing, using a Wafer Profiler CVP21 electrochemical capacitance voltage (ECV) system.

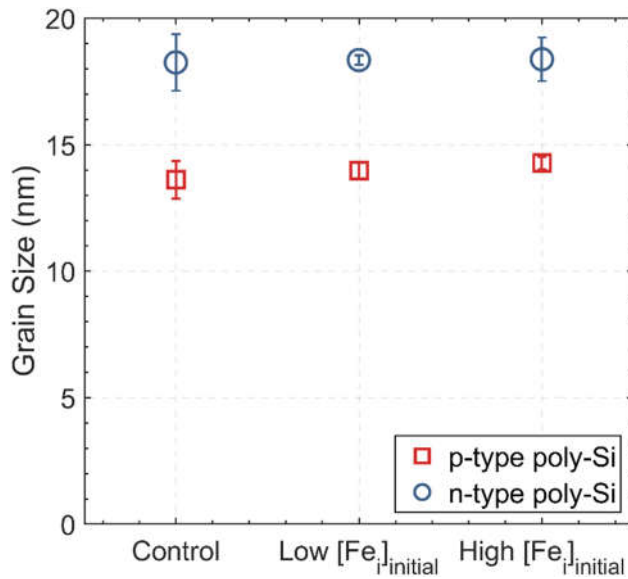


Figure S3. Grain size of the poly-Si/SiO_x structures with different initial bulk Fe concentrations: (control, [Fe]_i^{initial} = 2 × 10¹²cm⁻³ and [Fe]_i^{initial} = 1 × 10¹³cm⁻³). The crystalline properties were examined by grazing-incidence X-ray diffraction spectroscopy (GIXRD) using a PANalytical X'Pert PRO MRD system and the grain sizes of the poly-Si were calculated using the Debye–Scherrer formula based on the full width of half maximum (FWHM) of the peak at θ = 14.25°.

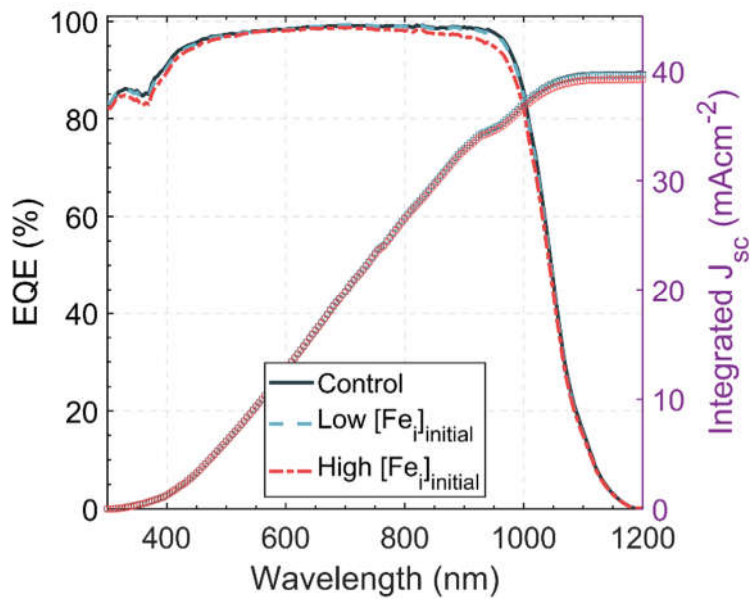


Figure S4. The EQE spectra and integrated J_{sc} values of the n-type front junction poly-Si/ SiO_x based cells with no (control), low ($[Fe]_{\text{initial}} = 2 \times 10^{12} \text{ cm}^{-3}$), and high ($[Fe]_{\text{initial}} = 1 \times 10^{13} \text{ cm}^{-3}$) Fe implantation doses.

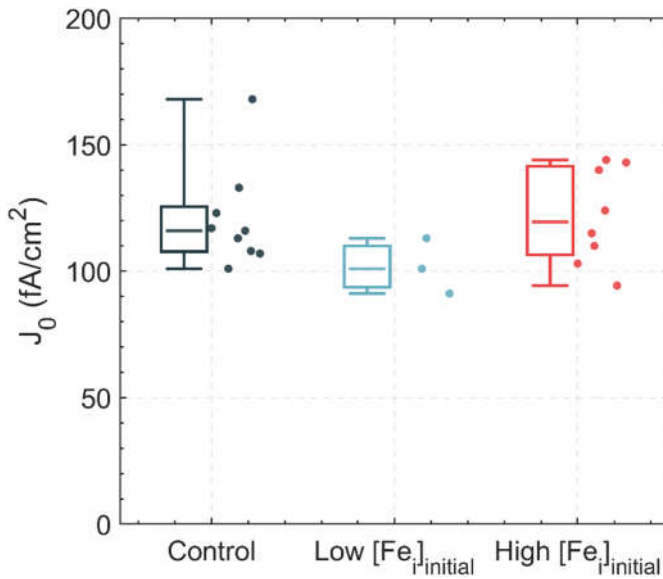


Figure S5. Measured double-side surface recombination current density (J_0) of the p-type front junction poly-Si/SiO_x based solar cells before metallization with no (control), low ($[\text{Fe}_i]_{\text{i}\text{i}_{\text{n}}\text{i}_{\text{t}}\text{a}} = 2 \times 10^{12} \text{ cm}^{-3}$), and high ($[\text{Fe}_i]_{\text{i}\text{i}_{\text{n}}\text{i}_{\text{t}}\text{a}} = 1 \times 10^{13} \text{ cm}^{-3}$) Fe implantation doses.

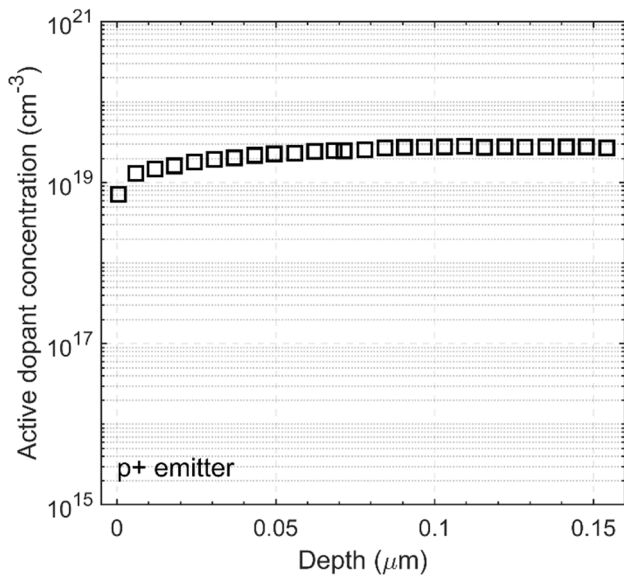


Figure S6. Measured active dopant profiles of boron in the p-type emitter of the n-type front junction poly-Si/SiO_x based solar cells, using a Wafer Profiler CVP21 electrochemical capacitance voltage (ECV) system.

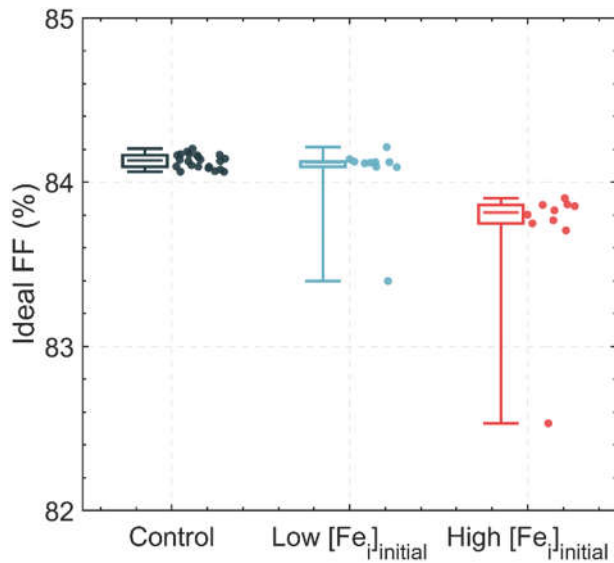


Figure S7. Ideal fill factor of the n-type front junction poly-Si/SiO_x based cells with no (control), low ($[Fe_i]_{initial} = 2 \times 10^{12} \text{ cm}^{-3}$), and high ($[Fe_i]_{initial} = 1 \times 10^{13} \text{ cm}^{-3}$) Fe implantation doses, based on the equation: $I = I_L - I_0 [\exp\left(\frac{qV}{nkT}\right)]$. The input parameters include open-circuit voltage V_{oc} , short-circuit current density J_{sc} , and an assumed ideality factor of $n = 1$.

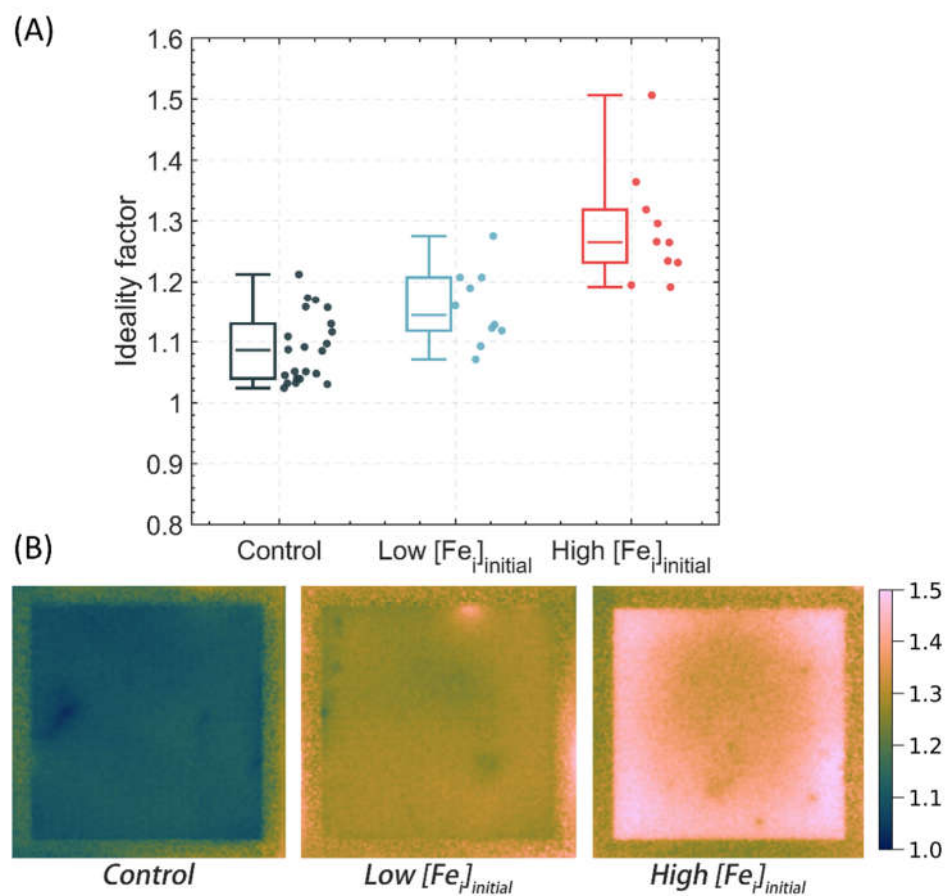


Figure S8. Ideality factor of the n-type front junction poly-Si/SiO_x based cells with no (control), low ($[Fe_i]_{initial} = 2 \times 10^{12} \text{ cm}^{-3}$), and high ($[Fe_i]_{initial} = 1 \times 10^{13} \text{ cm}^{-3}$) Fe implantation doses, extracted from (A) Sun-V_{oc} IV curve and (B) PL imaging (0.1-0.8 Sun).